A molecular mechanism for Wnt ligand-specific signaling

Authors:

Marie Eubelen[1,#], Naguissa Bostaille[1,#], Pauline Cabochette[1], Anne Gauquier[1], Patricia Tebabi[1], Andra C. Dumitru[2], Melanie Koehler[2], Philipp Gut[1,§], David Alsteens[2], Didier Y.R. Stainier[3], Abel Garcia-Pino[4,5] and Benoit Vanhollebeke[1,5,6,*]

Affiliations :

[1] Laboratory of Neurovascular Signaling, Department of Molecular Biology, ULB Neuroscience Institute, Université libre de Bruxelles (ULB), Gosselies B-6041, Belgium

[2] NanoBiophysics lab, Louvain Institute of Biomolecular Science and Technology, Université catholique de Louvain, 1348 Louvain-la-Neuve, Belgium

[3] Department of Developmental Genetics, Max Planck Institute for Heart and Lung Research, 61231 Bad Nauheim, Germany

[4] Laboratory of Cellular and Molecular Microbiology, Department of Molecular Biology, Université libre de Bruxelles (ULB), Gosselies B-6041, Belgium

[5] Walloon Excellence in Life Sciences and Biotechnology (WELBIO), Belgium

[6] Center for Microscopy and Molecular Imaging (CMMI), Université libre de Bruxelles (ULB), Gosselies B-6041, Belgium

[#] Equal contributions

[§] Current address: Nestlé Institute of Health Sciences, EPFL Innovation Park, Lausanne, Switzerland

[*] Correspondence to: Benoit.Vanhollebeke@ulb.ac.be

One sentence summary: How Wnt ligands achieve specificity

Abstract:

Cells can discriminate between multiple Wnt ligands. This Wnt decoding capacity has remained enigmatic as Wnt/Frizzled interactions are largely incompatible with mono-specific recognition. Intriguingly, Gpr124 and Reck enable brain endothelial cells to selectively respond to Wnt7. We show that Reck binds with low micromolar affinity to the intrinsically disordered linker region of Wnt7. Availability of Reck-bound Wnt7 for Frizzled signaling relies on the interaction between Gpr124 and Dishevelled. By polymerization, Dishevelled recruits Gpr124 and the associated Reck-bound Wnt7 into dynamic Wnt/Frizzled/Lrp5/6 signalosomes, resulting in increased local concentrations of Wnt7 available for Frizzled signaling. This work provides mechanistic insights into the Wnt decoding capacities of vertebrate cells and unravels structural determinants of the functional diversification of Wnt family members.

Main text:

Wnts constitute a large family of highly conserved and secreted proteins that mediate intercellular communication during animal development and in adult tissue homeostasis (*1, 2*). The ten members of the Frizzled (Fz) family are seven-pass transmembrane proteins that serve as receptors for Wnts (*3–5*). Greatly contributing to the complexity of Wnt signaling, the Wnt/Fz binding relationships are promiscuous, with multiple Wnts competing for binding to individual Fzs and *vice versa* (*3–12*). The Wnt/Fz contacts are indeed mediated by conserved residues or identical chemical modifications (*13*). These observations raise the question of how cells can respond to specific Wnt ligands when exposed to the overlapping expression patterns of multiple Wnt ligands that sometimes have opposing biological functions.

A pertinent example is the exclusive control of mammalian forebrain and ventral spinal cord angiogenesis by Wnt7a and Wnt7b (*14–16*). Specifically, in order to respond to neural progenitor-derived Wnt7 by activating Wnt/β-catenin signaling, endothelial cells must express Gpr124, an orphan member of the adhesion class of G protein-coupled receptors (*17–22*) as well as the GPI-anchored glycoprotein Reck (*22, 23*). Gpr124 and Reck physically interact to synergistically stimulate Wnt7-specific responses (*22, 24*) but it is unknown how Wnt7 signals are specifically recognized and transduced.

Reck is a Frizzled-independent Wnt7-specific receptor

We first sought to determine the Wnt7 recognition mechanism, a question inherently complicated by the ubiquitous expression of Fz receptors and their Lrp5/6 co-receptors in vertebrate cells. We therefore generated a set of mutant HEK293 cell lines by targeting (i) all ten *FZ* genes ($FZ_{1\text{-}10}^{-/-}$), (ii) *LRP5* and/or *LRP6* or (iii) *GPR124* and *RECK*, through multiplexed CRISPR/Cas9 mutagenesis (Fig. 1A and S1-3; see Methods). Ectopically

expressed Wnt7a-V5 could be immunodetected at the plasma membrane of WT, *FZ*$_{1\text{-}10}^{-/-}$ and *LRP5*$^{-/-}$*;LRP6*$^{-/-}$ cells, but not *GPR124*$^{-/-}$*;RECK*$^{-/-}$ cells (Fig. 1B). Ectopic restoration of Reck, alone or in combination with Gpr124, was sufficient to restore Wnt7a-V5 membrane labeling of *GPR124*$^{-/-}$*;RECK*$^{-/-}$ cells (Fig. 1C). As expected, Fz5 also bound Wnt7a-V5, reflecting the competence of this receptor to mediate baseline Wnt7 signaling (*11*, *24*). Control Wnt3a-V5 did not label WT or mutant cells (Fig. 1B and S4).

Proximity ligation assays (PLAs) in *GPR124*$^{-/-}$*;RECK*$^{-/-}$ cells confirmed the interaction between V5-tagged Wnt7a and HA-Reck or HA-Fz5 at the plasma membrane. The fraction of PLA-positive cells was identical (28.8 ± 7.5% and 28.3 ± 7.0%, respectively) but the intensity of the PLA signals generated with HA-Reck were 2-fold higher than with HA-Fz5 (Fig. 1D) (see Methods for quantification protocol). By contrast, HA-Gpr124 did not generate PLA signals. We tested all the Wnt family members and found that PLA interaction signals with HA-Reck were restricted to Wnt7a-V5 and Wnt7b-V5 (Fig. 1E), reflecting the specificity of the Gpr124/Reck complex for Wnt7 signaling (*20-22*, *24*).

We next determined that Reck recruits Wnt7a in the absence of Fz. We first performed PLAs between V5-tagged Wnt7a or Wnt3a secreted from WT cells and HA-Reck exposed at the surface of neighboring GFP-labeled *FZ*$_{1\text{-}10}^{-/-}$ cells. PLA signals were detected at the plasma membrane of 57.7 ± 17.4% of the GFP$^+$ cells in Wnt7a$^+$ co-cultures but were undetectable in Wnt3a$^+$ co-cultures (Fig. 1F). Accordingly, the co-culture of *FZ*$_{1\text{-}10}^{-/-}$ cells expressing Reck but not Gpr124$^{\Delta ICD}$ could drastically reduce Wnt7a-Fz5 signaling in neighboring Super Top Flash (STF) reporter cells (Fig. 1G). In contrast, none of the other tested Wnts, including Wnt3a (Fig. 1G), could be trapped by Reck-expressing cells (Fig. S5). Of note, in this ligand capture assay, Gpr124 was lacking most of its C-terminal ICD domain (residues 81 to 337 of the ICD, see Fig. 5E) to restrict the analysis to the extracellular parts of the Gpr124/Reck complex.

Defining the Reck-Wnt7 mono-specific recognition mechanism

Next, we mapped the domains of Reck required for Wnt7a binding. We generated a collection of HA-tagged single-domain deletion variants of Reck and, after determining that all variants reached the plasma membrane (Fig. S6), quantified Wnt7 PLA interaction signals. This analysis revealed that the N-terminal cysteine-knot domain (CK), and more particularly CK4 and CK5, were required for binding (Fig. 2A). Consistent with these results, Reck$^{\Delta CK4}$ was also inactive in competition assays (Fig. 1G).

Reck function in Wnt signaling is known to rely on its capacity to form a complex with Gpr124 through its CK domain (*20*, *22*), which we show to be required for Wnt7a binding. Although Gpr124 alone did not bind Wnt7 (Fig. 1B, 1D and 1G), we detected a 4-fold increase in Wnt7a-V5/HA-Reck PLA signals upon co-expression of untagged Gpr124 (Fig. 2B). In sum, these results suggest that Reck is a Fz-independent Wnt receptor, whose specific and exclusive binding to Wnt7 is reinforced by the interaction of Gpr124 with its CK domain (Fig. 2C) (*24*).

In order to better characterize the Reck/Wnt7 interaction, we modelled the 3D structure of Wnt7a based on *Xenopus* Wnt8a crystallographic analysis (*13*) (Fig. 2D). Wnt ligands adopt a two-domain structure reminiscent of a human hand pinching the globular Fz cysteine-rich domain (CRD, orange) via the palmitoylated 'thumb' of their N-terminal domain (NTD, cyan) and hydrophobic residues of their 'index' C-terminal domain (CTD, grey). The structures involved in Fz binding are pseudo-colored in orange in Fig. 2D. The two domains are connected through a flexible linker region of the NTD (purple).

We next generated a collection of Wnt7 variants deleted for specific domains or residues, or that carried domains from other Wnt ligands (Fig. 2E). Of note, all analyzed Wnt7 variants could be detected in the cell supernatant (Fig. S7). These ligands were each applied to PLAs,

and the resulting data showed that Reck binding occurs through the Wnt7a NTD. Wnt7a^{NTD} indeed bound Reck, while Wnt7a^{CTD} did not (Fig. 2F). Chimeric ligands made of Wnt7a^{NTD} fused to the CTDs of *Xenopus* Wnt8a (XWnt8a), murine Wnt4 or Wnt16 were also positive. The palmitoleic acid required for Fz binding was dispensable for the interaction with Reck as revealed by testing a Wnt7a^{S206A} palmitoylation mutant. Altogether, these binding assays reveal that Reck discriminates between Wnt ligands by recognizing a motif embedded in the Wnt7a NTD, at sites distinct from those engaged by Fz.

Smaller NTD variants lacking the linker region, Wnt7a$^{1-212}$ and Wnt7$^{1-237}$, did not bind Reck. This mutational analysis and the spatial segregation of the Wnt7a linker region from the Fz binding sites, suggest that Reck decodes Wnt7a, at least in part, through this linker. The linker, which is highly divergent amongst the different Wnt ligands, exhibits strong evolutionary conservation amongst the vertebrate Wnt7 orthologues (Fig. 2H and S8). This region is predicted to be intrinsically disordered (Fig. S9), a feature often found in molecular recognition elements providing the necessary structural plasticity to accommodate multiple partners, post-translational modifications or moonlighting functions. In many cases, intrinsically disordered regions also provide interactions with high specificity and moderate-to-high affinity (*26*).

Although *in situ* substitution of the XWnt8a linker by the Wnt7 linker (XW8a^{pWnt7a}) did not yield detectable PLA signals, presenting the Wnt7 linker at the free N-terminus of XWnt8a (pWnt7a-XW8a) was sufficient to confer Reck binding activity to XWnt8a (Fig. 2 E, F). We hypothesize that conformational alteration accounts for the lack of binding of XW8a^{pWnt7a}. In support of this hypothesis, reciprocal exchange of Wnt linkers between various Wnts abrogates their activity (Fig. S10).

To precisely map the Reck interaction site, we analyzed Gpr124/Reck-dependent STF signaling of 101 single residue variants of Wnt7a (Fig. 2G). The mutated residues correspond to surface-exposed NTD residues conserved between Wnt7a and Wnt7b, but not found in XWnt8a or other Wnt ligands. Residues were mutated to alanines, expect for endogenous alanine residues which were changed to arginine. While ~80% of the variants were as active as WT Wnt7a (>70% relative activity, green), eight Wnt7a variants (red) reduced Gpr124/Reck-dependent signaling to less than 10% (Fig. 2G). All but one (I37) critical residues clustered on the "top" or "back" of the predicted Wnt7a structure, with six mapping to the linker domain. All essential residues are strictly conserved amongst Wnt7 orthologues from fish to mammals and absent in other Wnts, including Wnt3a (Fig. 2H and S8).

The linker domain of Wnt3a has been shown to be essential for Wnt3a activity through Lrp6 binding (*27*). By analogy, the inactivity of the Wnt7 linker variants might therefore result from defective binding to Lrp5/6, Reck or both. In line with a function in Reck binding, $Wnt7a^{4A}$, a four-residue variant of Wnt7a (V241A/F251A/L252A/K262A) within the linker region (Fig. 4H), showed reduced Reck PLA signals as compared to WT Wnt7a. Of note, this lower activity occurred despite slightly improved secretion rates (Fig. 2I).

Biophysical characterization of the interaction between the Wnt7 linker domain and Reck

To investigate Reck-Wnt7 binding in a cell-free system, The CK domain of Reck (and variants thereof) were fused to the Fc domain of human IgG1. Fusion proteins were purified from HEK293T cells supernatants (Fig. 3A) and then titrated with synthetic pWnt7a and pWnt7b linker peptides by isothermal titration calorimetry (ITC). pWnt7a and pWnt7b bound Reck with affinity values of 7 μM and 1.2 μM, respectively (Fig. 3B and S11). As controls, the synthetic peptides corresponding to $Wnt7a^{4A}$ ($pWnt7a^{4A}$) as well as equivalent linker

peptides of Wnt3a (pWnt3a) showed no binding to Reck-CK-Fc. pWnt7b binding required Reck CK4 and CK5, but not CK1, CK2 or CK3, strikingly mirroring the PLA results in cultured cells (Fig. 2A). To corroborate the results provided by the ITC analysis, we used single molecule force spectroscopy (SMFS) to measure binding affinities at the single-molecule level (Fig. 3C). Binding of pWnt7b to Reck-CK-Fc was detectable with a measured Kd of 5 µM (Fig. 3D-F). Despite the fundamental differences between the two techniques, ITC and SMFS thus provided a close match between measured binding affinity values.

Altogether, while not excluding an additional role of the Wnt7 linker in Lrp5/6 binding (*27*), these data demonstrate that Wnt7 is recognized by Reck at least in part through its 'signature' linker motif. The moderate micromolar affinity values measured further suggest that after recognition of the linker, Reck establishes more extensive contacts with Wnt7, in a process that can be potentiated by Gpr124 (Fig. 2B).

Gpr124 function in Wnt7 signaling does not depend on its GPCR structure

Reck, by virtue of its GPI-anchoring mode, has limited potential to relay Wnt7 signals within the cell. Signal transduction therefore likely relies on other components of the receptor complex, *i.e.* Gpr124 and/or Fz/Lrp5/6 (Fig. 4A).

To uncover the signal transduction mechanism, we first evaluated the functional relationship between Gpr124 and Fz/Lrp5/6 complexes in cultured cells. Using the "Fz-free" and "Lrp5/6-free" cells (Fig. 1A), we found that the function of Gpr124/Reck strictly relies on Fz and Lrp5/6 (Fig. S12). We further established that their respective CRD and Dkk-1-sensitive Wnt ligand binding domains are essential, implying that Wnt7 binds and activates Fz/Lrp5/6 in a classical manner. If Reck mediates Wnt7 binding and Fz/Lrp5/6 trigger signaling, what underlies the essential function of Gpr124?

In the absence of Gpr124, Reck acts cell-autonomously as a potent inhibitor of Wnt7/Fz5 signaling, in a CK4-dependent manner (Fig. 4B). The inhibitory function of stand-alone Reck is particularly remarkable in light of the pool of membrane-associated Wnt7 in this Frizzled-positive setting (Fig. 4B). This observation implies that in the absence of Gpr124, Reck scavenges Wnt7 away from Fz5/Lrp5/6 complexes. Strikingly, the presence of Gpr124 switches Wnt7 signaling output from near complete inhibition to potent activation.

To establish how Gpr124 mediates this "on-off" Wnt7 signaling switch, we turned to the zebrafish model. Many Wnt processes, including the Wnt7/Gpr124/Reck-mediated cerebrovascular functions, are instructed at Wnt input levels only marginally above the signaling threshold values (*20*). It is therefore important to investigate the signal transduction pathway *in vivo*, in response to physiological Wnt7 inputs. The development of the zebrafish brain vasculature requires Reck/Gpr124 signaling, in a process of angiogenic sprouting that can readily be quantified. It therefore constitutes an ideal setting to perform structure-function analysis *in vivo* (*22, 29*). Using mRNA injections into one-cell stage *gpr124*$^{-/-}$ embryos (Fig. 4C), we evaluated the activity of three Gpr124 variants lacking the N-terminal extracellular part (Gpr124$^{\Delta ECD}$), the seven-span moiety (Gpr124$^{\Delta TM2-7}$) or the C-terminal cytoplasmic extension (Gpr124$^{\Delta ICD}$, residues 29-337 see Fig. 5E) (Fig. 4D). While ectopic expression of Gpr124$^{\Delta ECD}$ or Gpr124$^{\Delta ICD}$ did not restore brain angiogenesis in *gpr124* mutants or morphants, Gpr124$^{\Delta TM2-7}$ was sufficient to trigger brain angiogenesis *in vivo* (Fig. 4E, 4F and S13) and Wnt/β-catenin activity *in vitro* (Fig. S14).

This retained competence of Gpr124$^{\Delta TM2-7}$ was unexpected: Gpr124 is a GPCR, a receptor super-family classically relaying extracellular stimuli by ligand-induced conformational remodeling of their seven transmembrane spans, which are absent in the engineered Gpr124$^{\Delta TM2-7}$. These data raise the possibility that Gpr124 does not act as a "classical" GPCR when promoting Wnt7 signaling.

To test this hypothesis, we developed a bimolecular complementation assay in which the GPR124 ECD and ICD are linked by a surrogate anti-GFP VhhGFP4 nanobody-GFP connector (Fig. 4G). Nanobodies are single-domain antibody fragments that have been used to (mis)-rout intracellular proteins (*30*). We re-purposed them here as conditional tethers for signal transduction analysis. The highly-flexible GFP-VhhGFP4 connector acts a buffering module ensuring that conformational information cannot be exchanged between tethered partners. Based on this idea, we designed Gpr124 $^{\Delta ICD}$-GFP and Gpr125 $^{\Delta ICD}$-GFP fusions to which VhhGFP4-fusions will be recruited (Fig. 4G, S15). Notably, the *gpr124* vascular phenotypes were partially suppressed by co-injecting mRNAs encoding Gpr124$^{\Delta ICD}$-GFP and VhhGFP4-ICD (residues 29-337) (Fig 4H). Moreover, a chimeric Gpr124 ECD linked to cytoplasmic GFP *via* the transmembrane span of the unrelated CD27 receptor was similarly active with VhhGFP4-ICD (Fig 4G and H). We used Gpr125, a closely related aGPCR devoid of angiogenic activity, as well as VhhGFP4-RFP as negative controls (*20-22*).

These results confirm the surprising finding that Gpr124 function in Wnt7 signaling does not require signal transduction across the membrane through conformational remodeling. Instead, Gpr124 seemingly acts in this module as a signaling-deficient transmembrane protein whose activity relies on its Reck-binding ECD (*22*, *24*) and its conformationally uncoupled ICD. The function of this latter domain remaining to be defined (Fig. 4I).

Gpr124 activity requires Dishevelled binding

We hypothesized that the Gpr124 ICD might operate through Dishevelled (Dvl), the necessary effector of Wnt signaling which interacts with Fz. This 'Dvl hypothesis' is rooted in the findings that Gpr125 physically interacts with Dvl via its C-terminal ICD domain (*31*) and that Gpr124/125 hybrids in which the ICD of Gpr124 is replaced with the ICD of Gpr125 are able to promote brain angiogenesis (Fig. 5A) (*22*). Gpr124/Fz2 hybrids (Gpr124^{ICDFz2})

harboring the Fz2 ICD, which is known to bind Dvl, were similarly active. In contrast, full-length Fz2 was not. Notably, the activity of Gpr124^{ICDFz2} was dependent on its KTxxxW and ETTV Dvl binding motifs (Fig. 5A).

Moreover, in a non-canonical Wnt signaling context, over-expression of Gpr125 impairs convergence and extension movements during zebrafish gastrulation, resulting in a mediolateral broadening of the AP embryonic axis as well as synophthalmia or cyclopia (*31*). These phenotypes were linked to the capacity of Gpr125 to modulate Dvl distribution through its ICD. Strikingly, Gpr124 strictly mimicked Gpr125 in these settings (Fig. 5B, Fig. S16).

We therefore tested whether Gpr124 affects the intracellular distribution of Dvl. We used two distinct cell populations of the zebrafish blastula to address this question: the superficial enveloping cell layer (EVL), where cells maintain continuous intercellular contacts, and the deep layer cells (DEL), which establish more discrete intercellular junctions (Fig. 5C). Gpr124-tagRFP distribution reflects this differing junctional organization, with near-uniform and discontinuous membrane signals in EVL and discontinuous signals in DEL cells (Fig. 5C). When expressed individually, *Xenopus* Dvl-GFP mainly formed cytoplasmic punctae in both cell populations, as reported previously (*31*). Co-expressing Gpr124-tagRFP largely redistributed Dvl-GFP to the Gpr124-positive membrane subdomains in both EVL and DEL cells, where the proteins co-localized (Fig. 5D).

We generated a collection of Gpr124 truncation variants with a range of deletions within the 337 amino acid-long ICD (Fig. 5E), and evaluated their Wnt7/β-catenin functions *in vitro* (Fig. 5F) and *in vivo* (Fig. 5G). The Gpr124 and Gpr125 ICDs contain no obvious motifs except for the last four ETTV amino acids that constitute a canonical PDZ binding motif (PBM), also found in a subset of Fz receptors. The ETTV tetrapeptide contributed, but was not essential, for Gpr124 activity. It was similarly dispensable for high-dose Gpr124 or

Gpr125-induced planar cell polarity phenotypes (*31*) (Fig. S16). Analysis of increasingly larger C-terminal deletion variants mapped the essential region of the Gpr124 ICD to the interval spanning residues 81 to 213. Notably, the activity of the different ICD variants exactly matched their capacity to recruit Dvl-GFP in EVL cells (Fig. 5H) and $FZ_{1\text{-}10}^{-/-}$ cells (Fig. 5I). This interaction between Gpr124 and Dvl could also be detected by co-immunoprecipitation. In these assays, only Gpr124 variants harboring the 81-213 region interacted with exogenous Dvl-GFP (Fig. 5J) or endogenous DVL2 (Fig. S17) in $FZ_{1\text{-}10}^{-/-}$ cells. This interaction is likely direct as purified recombinant GST-Gpr124-ICD or GST-Gpr124-ICD$^{\Delta ETTV}$ fusion proteins were able to pull-down *in vitro* translated Dvl-GFP (Fig. S18), as previously reported for Gpr125 (*31*).

To test for the endogenous requirement for Gpr124 ICD interaction with Dvl, we performed gene disruption experiments in somatic zebrafish embryos by co-injecting *zCas9* mRNA and sgRNAs targeting the Gpr124 coding sequence immediately upstream, within or downstream of the Dvl binding region (ICD residues 81-213). While the injection of four out of five sgRNAs predicted to disrupt Dvl recruitment to Gpr124 generated embryos lacking hindbrain CtAs with a penetrance ranging from 13.6 to 70.8%, none of the seven sgRNAs targeting Gpr124 downstream of the Dvl binding region generated significant brain vascular defects (Fig. 5K).

Taken together, these experiments identify Dvl as a Gpr124 binding partner that could mediate its Wnt7 signaling activities at the plasma membrane. Unlike Fz, Gpr124-mediated recruitment of Dvl at the plasma membrane did not yield a detectable increase in phosphorylated Dvl levels, an early indicator of Wnt signaling activation upstream of β-catenin stabilization (*32, 33*) (Fig. S19). This absence of Gpr124-induced Dvl activation is consistent with the experiments shown in Fig. 4D-I that showed Gpr124 to be a conformationaly inert Wnt7 signaling mediator.

Dvl polymers assemble ligand-specific Wnt signalosomes by linking Gpr124 and Fz

Knockdown of *DVL2* by siRNA impairs Gpr124/Reck-mediated signaling (Fig. S20). As Dvl is an essential adaptor of Fz, and Gpr124/Reck signaling relies on Fz (Fig. S12), such cell-wide loss-of-function approaches are however of limited value to probe Dvl function specifically as a Gpr124 (and not Fz) effector. We therefore used the nanobody strategy described in Fig. 4G to selectively modulate Dvl binding to Gpr124. Strikingly, VhhGFP4-mediated recruitment of Dvl to Gpr124$^{\Delta ICD}$-GFP, but not to Gpr125$^{\Delta ICD}$-GFP, was sufficient to partially reverse the *gpr124* mutant vascular phenotype *in vivo* (Fig. 6A). As additional control, injecting either component alone or substituting VhhGFP4-Dvl with VhhGFP4-RFP did not rescue brain angiogenesis. These experiments reveal that Dvl is sufficient to mediate Gpr124 intracellular functions in Wnt7 signaling.

Gpr124, Reck and Fz/Lrp5/6 have been reported to form higher-order receptor complexes (*24*). We reasoned that the Gpr124 ICD might assemble this complex via Dvl. Dvl molecules indeed assemble signalosomes through dynamic polymerization (*34-36*). As Dvl physically interacts with both Gpr124 and Fz, Gpr124 and the associated Reck-bound Wnt7 might thus become trapped in dynamic Wnt signalosomes, thereby increasing the local concentration of Wnt7 ligands available for Fz signaling.

Wnt signalosomes are readily detected by light microscopy as large, punctate structures enriched in Dvl that form at or below the plasma membrane (*35–37*). To determine whether Fz and Gpr124 co-distribute in Wnt signalosomes in a Dvl-dependent manner, the localization of individually expressed Fz-GFP and Gpr124-tagRFP was first examined in DEL cells. Fz4 decorated the entire plasma membrane periphery while, in contrast, Gpr124-tagRFP accumulated at cellular contacts (Fig. 6B, 5C, 5D). This differential membrane localization was retained upon Dvl expression (Fig. 6B). Consistent with their Dvl binding capacity, both

receptors recruited Dvl-GFP from the cytoplasm (Fig. 5C) to their respective membrane compartments (Fig. 6C). However, when Gpr124-tagRFP and Fz4-GFP were co-expressed, Fz4-GFP quantitatively relocalized, in a Dvl-dependent manner, to the Gpr124-positive intercellular junctions (Fig. 6D). Gpr124-tagRFP and Fz4-GFP colocalized in Wnt signalosome-reminiscent punctate structures that were particularly evident at EVL cell membranes (Fig. 6E and Fig. S21).

We used bimolecular fluorescence complementation as an additional assay to test for Dvl-dependent Fz/Gpr124 interaction in DEL cells. Co-injection of Gpr124-VN_{155} (I152L) and Fz1-VC_{155} indeed generated bright junctional signals in a Dvl-dependent manner (Fig. 6F), demonstrating that Fz and Gpr124 indirectly interact via the Dvl scaffold protein. Altogether, these data provide a molecular mechanism for spatial enrichment of Wnt7 within Fz/Lrp5/6 signalosomes, permitting potentiated and ligand-selective cellular responses (Fig. 6G).

Discussion

In summary, this work provides mechanistic insights onto the Wnt decoding capacities of vertebrate cells. It also demonstrates that the evolutionarily constrained Wnt structure retained enough diversity to allow ligand-specific cellular responses, a property so far thought to require structurally unrelated Frizzled ligands like Norrin (*38*).

These structural insights into Wnt evolution and function suggest that additional Wnt decoding modules exist, enabling fine-tuning of cellular behaviors in response to other Wnt or Fz family members. The discrete interaction mode of Fz and Wnt leaves large surfaces made of evolutionary conserved residues available to accommodate additional co-receptors. We therefore propose that Wnt decoding modules might have contributed to shaping the evolution of the Wnt ligand family.

The benefit to promiscuous Wnt/Fz interactions with specificity conferred by accessory proteins rather than mono-specific Wnt/Fz interactions might lie in the increased modularity offered by the binary system. A single-component system would be limited to an on or off signaling output. The two-component system described here can, context-dependently, achieve cell-autonomous Wnt signaling inhibition or act as a tunable rheostat amplifying the signaling output of specific Wnt ligands.

A salient molecular property of the Wnt7 module is the use of Dvl as common Gpr124 and Fz adaptor. It is tempting to propose that taking advantage of Fz-associated scaffold proteins like Dvl could constitute a generic mechanism for Wnt/Fz modifiers. Accordingly, cells recurrently tailor their responses to Wnt by reshaping the molecular composition of the Dvl-associated proteins, including regulatory kinases, E3 ubiquitin ligases and components of the endocytic machinery (*34-36*).

Our findings have clinical implications. The pleiotropic functions of Wnt signaling in health and disease make this pathway a conspicuous yet intrinsically challenging therapeutic target. Manipulating the Wnt/β-catenin pathway at the level of its cytosolic or nuclear components harbors high potential for systemic effects with undesirable outcomes across a range of tissues (*39*). Interventions focused on specific Wnts, Fz receptors or other signaling components at the cell membrane might, in principle, be more selective and hence better positioned to lead to clinically viable strategies (*4, 40-42*). The mechanism uncovered here expands the prospects for specific Wnt-targeted interventions. In particular, by giving molecular insights at the heart of Wnt7-specific signaling, it provides an unprecedented opportunity for the targeted treatment of human brain disorders with neurovascular involvement, including stroke and brain cancer (*43*).

Acknowledgments:

We thank Jeremy Nathans (Johns Hopkins), Roel Nusse (Stanford) and Vladimir L.Katanaev (UNIL) for advice and fruitful discussions. **Funding:** M.E. and N.B. are FRIA fellows from Fonds de la Recherche Scientifique - FNRS. P.C. and D.A. are Postdoctoral Researcher and Research Associate of the FRS.-FNRS, respectively. Work in the B.V. laboratory is supported by the FNRS (MIS F.4543.15), the Concerted Research Action (ARC), the Fondation ULB, the Queen Elisabeth Medical Foundation (Q.E.M.F.) and the FRFS-WELBIO (CR-2017S-05). The CMMI is supported by the European Regional Development Fund and the Walloon Region. **Author contributions:** All authors performed research and/or analyzed data. B.V. designed research and wrote the manuscript. All authors discussed results and edited the manuscript. **Competing interests:** The ULB (B.V.) has filed a patent on the neurological applications of the Gpr124/Reck-mediated signaling mechanism. **Data and materials availability:** All data are available in the main text or the supplementary materials.

Supplementary Materials

Figs. S1 to S22

Table S1

Materials and Methods

Zebrafish lines

Zebrafish (*Danio rerio*) were maintained at 28 °C on a 14 h light/10 h dark cycle. Embryos were obtained and raised under standard conditions in accordance with European and national ethical and animal welfare guidelines (protocol approval number: CEBEA-IBMM-2017-22:65). Staging was performed according to Kimmel et al. (*44*). The transgenic and mutant lines used in this study are *Tg(kdrl:EGFP)*^{s843} (*45*), *Tg(kdrl:HRAS-mCherry)*^{s896} (*46*) and *gpr124*^{s984} (*22*).

Morpholinos, RNA constructs and microinjection

Splice-blocking morpholinos targeting *gpr124* (ACTGATATTGATTTAACTCACCACA) (*22*) were purchased from Gene Tools and injected at the one-cell stage at 2 ng. Synthetic mRNAs were transcribed from NotI linearized pCS2 using the mMessage mMachine SP6 Kit (Thermo Fisher Scientific) and injected into one-cell stage zebrafish embryos.

Somatic gene disruption in zebrafish by CRISPR/Cas9

The *gpr124*^{ICD}-targeting sgRNA*s* constructs (sgRNA 1-12) were obtained by *in vitro* annealing of the following primers (1-Fo: TAGGTGGCATGCTACAAAAAGC and 1-Rv: AAACGCTTTTTGTAGCATGCCA ; 2-Fo: TAGGTTTGGGTCCGTAGGTGGA and 2-Rv: AAACTCCACCTACGGACCCAAA ; 3-Fo: TAGGGTAATGGTTTGGGTCCGT and 3-Rv: AAACACGGACCCAAACCATTAC ; 4-Fo: TAGGAGAAGAAGAGTAATGGTT and 4-Rv: AAACAACCATTACTCTTCTTCT; 5-Fo: TAGGAAGCTTGTAGTAGAACCA and 5-Rv: AAACTGGTTCTACTACAAGCTT; 6-Fo: TAGGCCATTCTGGCCCTCTGAA and 6-Rv: AAACTTCAGAGGGCCAGAATGG; 7-Fo: TAGGCCAACGGGCGGCACAGAG and 7-Rv: AAACCTCTGTGCCGCCCGTTGG ; 8-Fo: TAGGGGCACAGAGGGGAAGGAC and 8-Rv : AAACGTCCTTCCCCTCTGTGCC ; 9-

Fo: TAGGTAGTGATGGAGGTAGCAG and 9-Rv : AAACCTGCTACCTCCATCACTA ; 10-Fo: TAGGTGCCTTCGGTAGCACGTA and 10-Rv : AAACTACGTGCTACCGAAGGCA ; 11-Fo: TAGGGGTATGAAGAGCAGGGTA and 11-Rv : AAACTACCCTGCTCTTCATACC ; 12-Fo: TAGGTCGGTGGGTATGAAGAGC and 12-Rv : AAACGCTCTTCATACCCACCGA) and cloning into pT7-gRNA (Addgene #46759), as described in (*47*). sgRNA were transcribed from the BamHI linearized vector pT7-gRNA using the MEGAshortscript T7 kit (Thermo Fisher Scientific). The synthetic Cas9 mRNA was transcribed from the XbaI linearized vector pT3TS-nls-zCas9-nls (Addgene #46757) using the mMessage mMachine T3 Kit (Ambion). sgRNAs 1-12 (50 pg) and nls-zCas9-nls mRNA (150 pg) were injected into one-cell stage zebrafish embryos. The brain vasculature was analyzed and imaged at 48 hpf.

Whole-mount *in situ* hybridization (WISH)

Digoxigenin-labeled antisense riboprobes were synthesized with the digoxigenin (DIG) RNA labeling kit (Roche Diagnostics GmbH). Embryos were fixed in 4% paraformaldehyde overnight at 4°C and whole-mount *in situ* hybridization was performed using digoxigenin-labeled *myod1* riboprobes as previously described (*48, 49*).

Expression plasmid constructs

Wnt, Frizzled, Reck and Gpr124 and their variants used in STF and PLA assays were expressed from the CMV promoter of the pCS2 plasmid except for the following plasmids: pRK5-Lrp5-rhotag, Fz4-GFP (Addgene #42197), Fz1 (Addgene #42253) and Fz5 (Addgene #42267), all kindly provided by J. Nathans. Single-point mutation variants, deletions and chimeras were generated using In-Fusion cloning (ST0345, Takara) and tandem overlapping PCR products. All constructs were confirmed by Sanger sequencing. Throughout this study, we used *Xenopus* Dvl-GFP (Addgene #16788, from the R. Moon laboratory), zebrafish Gpr124 and Gpr125 as well as mouse Reck and untagged Wnt ligands (*22*). The collection of

active human Wnt-V5 ligands was kindly provided by the Xi He laboratory *via* Addgene (#43807 to #43825) (*50*). The activity of the V5-tagged ligands was verified by STF assays (Fig. S22). Reck deletion variants correspond to the following amino acids of mouse Reck (NP_057887.2): Reck$^{\Delta CK1}$: 46-93; Reck$^{\Delta CK2}$: 113-150; Reck$^{\Delta CK3}$: 160-206; Reck$^{\Delta CK4}$: 225-272; Reck$^{\Delta CK5}$: 301-347; Reck$^{\Delta CK1-5}$: 46-347; Reck$^{\Delta CRD}$: 352-484 and Reck$^{\Delta KAZAL}$: 636-798. Gpr124 deletion variants correspond to the following amino acids of zebrafish Gpr124 (NP_001305000.1): Gpr124$^{\Delta ECD}$: 68-725 and Gpr124$^{\Delta TM2-7}$: 764-1030. The Gpr124 ICD used in deletion, swapping or fusion constructs corresponds to residues 1058-1367 of the full length protein (28-337 of the ICD), unless otherwise indicated. The ICD of Gpr124 is defined as the segment that follows the last transmembrane segment of the seven pass transmembrane protein as non-ambiguously defined by the InterPro server of EMBL-EBI (based on the Phobius transmembrane topology and signal peptide predictor from the Stockholm Bioinformatics Centre). The ICD of zebrafish Gpr125 (NP_001289153) and of zebrafish Fz2 (NP_571215.1) were similarly defined and correspond to the residues 1054-1346 and 526-550, respectively. Gpr124^{ECD}-TM^{CD27}-GFP was generated by replacing the 7-TM span of Gpr124 (residues 743-1030) by the TM of mouse CD27 (NP_001028298.1) (IFVTFSSMFLIFVLGAIL). The VhhGFP4-ICD construct was generated by fusing the Gpr124 ICD to the C-terminus of VhhGFP4 (kindly provided by Markus Affolter (*30*)). Gpr124$^{ICDFz2\Delta KTxxxW/\Delta ETTV}$ was generated by deleting the KTxxxW (KTLHSW) and ETTV motifs within the ICD of zebrafish Fz2. The BiFC constructs were subcloned from pBiFC-VC155 (Addgene #22011) and pBiFC-VN155 (I152L) (Addgene #27097). The HA tag was inserted after residue 22 in murine Reck, residue 47 in zebrafish Gpr124 and residue 22 in murine Fz5. The FLAG tag was inserted after residue 47 in zebrafish Gpr124. We thank the numerous colleagues that facilitated this work by depositing their plasmids at Addgene.

Cell culture and HEK293(T) mutant cell lines

HEK293T cells were obtained from ATCC (CRL-3216) and the HEK293 STF cell line was kindly provided by J. Nathans. WT and mutant cells were cultured in DMEM/F12 medium (Lonza) supplemented with 10% fetal bovine serum and maintained at 37°C in a humidified incubator equilibrated with 5% CO_2. *GPR124* and *RECK* were genetically inactivated using CRISPR/Cas9 approaches in HEK293 STF cells and *LRP5*, *LRP6* and *FZ* were inactivated in HEK293T cells. The mutant cell lines were obtained by the iterative CRISPR/Cas9-mediated mutagenesis strategy illustrated in Fig. 1A. CRISPR/Cas9 guide sequences were designed using the http://crispr.mit.edu/ website and were cloned into pSpCas9(BB)-2A-GFP (*42*). The top 1% of GFP^+ cells was isolated by FACS (AriaIII, BD Biosciences) 48 h after transfection and distributed in 96-well plates for clonal expansion. In order to facilitate the genetic characterization of the mutant cell lines, clones generating multiple-peak derivative melt curves in high-resolution melt analyses were first counter-selected. For each gene, two independent PCR products flanking the target site (300-1000 bp PCR products centered on the PAM site) were gel purified and characterized by Sanger sequencing on both strands. The absence of WT alleles in the uncloned PCR product was verified and the number of different edited alleles (1, 2 or 3 in hypotriploid HEK293 cells) was deduced from the complexity of the chromatograms (Fig. S1). For each gene, the two independent PCR products were then cloned in pCR™-Blunt II-TOPO® (Thermo Fisher Scientific) and individual colonies were sequenced until each edited allele was sequenced at least twice from each individual PCR amplicon. The number of analyzed colonies for the $FZ_{1\text{-}10}^{-/-}$ cell line is provided in Table S1. The sequencing chromatograms form the identified individual clones were then aligned to ensure that the allelic complexity of the uncloned PCR can exhaustively be accounted for by the identified alleles (Fig. S1). Finally, to exclude allelic exclusion by PCR amplification bias, the absence of WT alleles in the $FZ_{1\text{-}10}^{-/-}$ cell line was verified by whole exome sequencing.

STF dual luciferase assay

Cells were plated into 96-well plates and transfected after 24 h in triplicate with Lipofectamine 2000 (Thermo Fisher Scientific). The amount of plasmid DNA transfected per well was optimized for each expression vector as follows: Renilla luciferase (0.5 ng), Wnt ligands (20 ng), Fz receptors (5 ng), Lrp5 (2.5 ng), Gpr124 (10 ng), Reck (5 ng) and Dkk-1 (10 ng) unless otherwise indicated. The total amount of DNA was adjusted to 100 ng per well with the empty pCS2 vector. Dual luciferase assays were performed using the STF cell line or by co-transfecting 20 ng of M50 Super 8x TOPFlash plasmid (Addgene #12456). Cells were harvested in passive lysis buffer (E1980, Promega) and the activities of the Firefly and Renilla luciferases were measured sequentially using the Dual-Luciferase Reporter Assay system (E1980, Promega) 48 h post transfection. The competition assays in Fig. 1G and Fig. S5 were performed by plating cells as a 1:1:1 mixture at 90% confluency in 96-well plates 24 h after transfection. Luciferase activity was measured 24 h after co-culture. For siRNA, cells were plated into 96-well plates and transfected after 24 h in triplicate using Lipofectamine 2000 (Thermo Fisher Scientific) with 1 pmol (per well) of *Dvl2* or control siRNAs (SASI_HS01_00104204 and SIC001, Sigma-Aldrich) together with the indicated plasmids.

Immunofluorescence and proximity ligation assay

Cells were grown in glass-coated chambers (IBIDI) and transfected after 24 h with Lipofectamine 2000 (Thermo Fisher Scientific). Cells were fixed with 4% paraformaldehyde for 10 min at room temperature (RT) 48 h post transfection. For immunofluorescence staining (IF), cells were blocked in 1% BSA-PBS for 30 min before being exposed to primary antibodies for 1 h at RT. After three PBS washes, cells were incubated with secondary antibodies for 1 h at RT. For anti-V5 staining of Wnt ligands, cells were additionally washed for 10 min in PBS 0.1% Tween 20 before incubation with the secondary antibody solution. For the proximity ligation assay (PLA) (Sigma-Aldrich), cells were blocked for 30 min at

37°C with the Blocking solution provided by the manufacturer before being incubated with the primary antibodies for 1 h at RT. Cells were washed three times and incubated with the PLA probes anti-rabbit PLUS and anti-mouse MINUS for 1 h at 37°C. After two PBS washes, cells were incubated with the Duolink Ligation solution for 30 min at 37°C. After two PBS washes, cells were incubated with the Duolink Amplification solution for 100 min at 37°C. The following antibodies were used: monoclonal mouse anti-V5 (R96025, Thermo Fisher Scientific) at 1:500 for IF and PLA, purified polyclonal rabbit anti-HA (H6908, Sigma-Aldrich) at 1:400 for IF and PLA and anti-mouse Alexa488-conjugated secondary antibody (Thermo Fisher Scientific) at 1:5000. Cells were stained for 2 min with Hoechst diluted to 10 $\mu g\ ml^{-1}$ in PBS.

Western blot, Dot blot, GST pull-down and co-immunoprecipitation

The following antibodies were used with an overnight incubation at 4°C: rabbit anti-DVL2 (1:1000, #3224S, Cell Signaling Technology), rabbit anti-DVL2-phospho T224 (1:1000, ab124941, Abcam) and mouse monoclonal anti-β-actin-peroxidase (1:50000, A3854, Sigma-Aldrich), chicken anti-GFP (1:5000, GFP-1010, Aves) and mouse monoclonal anti-FLAG M2 (1:1000, F1804, Sigma-Aldrich).

Dot blot analyses were performed according to manufacturer's protocol with a BioDot SF apparatus (Bio-Rad). Serial dilutions of supernatant were spotted onto a nitrocellulose membrane (GE Healthcare). After drying, the membrane was incubated with the antibodies as described above. For the co-immunoprecipitations assays, HEK293T were collected 48 h after transfection from six-well plates and resuspended after two PBS washes in lysis buffer (150 mM NaCl, 25 mM Tris (pH 7.5) and 1% IGEPAL CA-630 (Sigma-Aldrich)) containing EDTA-free protease inhibitor cocktail (Roche) for 30 min at 4°C. After centrifugation at 20000g for 10 min, the supernatant was incubated with 20 µl of anti-FLAG M2 affinity gel

(A2220, Sigma-Aldrich) overnight at 4°C. Beads were washed five times with the lysis buffer and boiled in 2x Laemmli Sample buffer. For GST pull-downs, the coding sequence of Gpr124 ICD and its ΔETTV variant were fused downstream of GST sequences into pGEX-6P1 (GE Healthcare). The GST-fusion proteins were induced in *Escherichia coli* BL21 by exposure to 0.1 mM of IPTG in LB medium at 37°C for 4 h. Cells were subsequently lysed in a cell disruptor (M110S, Microfluidics) and after centrifugation, the GST-fusion protein from the supernatant were immobilized on Glutathione Sepharose beads (17-0756-01, GE Healthcare). The Dvl-GFP and GFP constructs were transcripted using the mMESSAGE mMACHINE SP6 Transcription Kit (Thermo Fisher Scientific) and *in vitro* translated using the Rabbit Reticulocyte Lysate System provided by Promega (L4960) in the presence of S^{35}-methionine (NEG009T001MC, PerkinElmer). The beads were incubated with the radiolabeled proteins in PBS for 3 h at 4°C with gentle mixing and then washed five times with cold PBS. The bound complex was resuspended in 2x Laemmli buffer, separated by SDS-page and analyzed by fluorography.

Microscopy and images processing

Cells and zebrafish embryos were imaged with a LSM710 confocal microscope and images were processed in ImageJ. Images of eye fusion phenotypes were taken on a Leica M165 FC. Brain vasculature renderings were generated using Imaris software (BitPlane).

The following method was used for the quantification of the PLA signal: The *in situ* PLA signals are seen as bright fluorescent dots of characteristic appearance. The signal lined the cell surface, as expected given the membrane localization of the receptors. For quantification, several images were acquired on LSM710 confocal microscope with a 20x objective. ImageJ was used to determine the ratio of the total area occupied by the PLA-positive pixels to the DAPI-positive pixels, the latter being indicative of the number of cells in the field of view. On the dot plot, each dot represents the ratio of one image. Each image typically contained 50-

100 cells.

Structural modeling

The structure of *Xenopus* Wnt8a (PDB ID: 4F0A) (*13*) was used as a starting model for Wnt7a. Missing residues and substitutions were modeled using the program Modeller (*51*). The modeling strategy included accounting for existing disulphide bridges as observed in XWnt8a. The initial best models were subjected to a conjugate-gradient energy minimization in vacuum with the Cα restrained and then freed in a second minimization step. These models were then embedded in a water box and electric neutrality was achieved by adding Na^+ counter ions at 150 mM. The whole system was again energy minimized in 3000 steps. The molecular dynamics simulation was carried out for 0.5 ns with the program NAMD 2.7 at constant temperature (310 K) and constant pressure (1 atm), with periodic boundaries and using CHARMM36 as force field (*52*). A time step of 2 fs was used to integrate the equations of motion. The short-range interactions were cut at 12 Å and the smooth-particle mesh Ewald method was used to calculate electrostatic interactions. Hydrogen atoms were constrained using the SHAKE algorithm. The resulting model is an average representation of the stable simulation.

Recombinant Reck-Fc fusions and synthetic peptides

The HA-tagged CK domain of Reck and its individual CK motif deletion variants were fused at the N-terminus of the Fc region of human IgG1. The fusion vector was kindly provided by J. Nathans (*24*). Fc fusion proteins were recovered in serum-free FreeStyle 293 Expression Medium (Thermo Fisher Scientific) from the supernatant of HEK293T cell cultures 72 h post transfection with Lipofectamine 2000 (Thermo Fisher Scientific). After collection, the supernatants were submitted to Protein G affinity purification (Protein G Sepharose 4 Fast Flow, Sigma-Aldrich). After acidic elution, protein purity was assessed by Coomassie Blue

staining (Fig. 3A). Synthetic Wnt linker peptides were obtained from Chinapeptide Co., Ltd at purities of over 90%.

Isothermal titration Calorimetry

ITC titrations were carried out on an Affinity ITC (TA Instruments). Prior to the measurement, Reck-CK-Fc and all Reck-CK-Fc fusions were dialyzed to Tris-NaCl buffer (50 mM Tris pH8, 300 mM NaCl). In each case Wnt-derived peptides were prepared with buffer from the last step of protein dialysis. The samples were filtered and degassed before being examined in the calorimeter and the titrations were performed at 25°C. All the experiments consisted of injection of constant volumes of 2 µL of titrant into the cell (200 µL) with a stirring rate of 75 rpm. Nominal sample concentrations were between 20 µM and 40 µM in the cell and 400 µM to 1.0 mM in the syringe. Actual sample concentrations were determined after dialysis or buffer exchange by measurement of their absorption at 280 nm or by the BCA method. All data were analyzed using the MicroCal Origin ITC 7.0 and NanoAnalyze software packages.

Atomic force microscopy

Glass coverslips coated with a thin gold layer were cleaned in an ultraviolet radiation and ozone (UV-O) cleaner (Jetlight) for 15 min and subsequently immersed overnight in an ethanol solution containing 1 mM 16-mercaptododecahexanoic acid and 1-mercapto-1-undecanol at a 1:99 volumetric ratio. Substrates were then rinsed with ethanol, dried with N_2 and added to a solution containing equal volumes of 20 mg ml^{-1} *N*-hydroxysuccinimide (NHS) and 50 mg ml^{-1} 1-ethyl-3-(3-dimethylaminopropyl)-carbodiimide (EDC) for 30 min. The obtained NHS activated surfaces were rinsed with ultrapure water and incubated with 100 µl of a 10 µg ml^{-1} Protein G solution for 1 h at RT. Samples were then washed with washing buffer (3 x 5 min) and further incubated with 100 µl blocking buffer for 1 h at RT. Finally, 50

µl of a 0.2 µg ml^{-1} Reck-CK-Fc solution was added to the substrates for 1 h, rinsed with washing buffer and subsequently used for AFM experiments. Single-molecule force spectroscopy (SMFS) measurements were performed in PBS buffer at RT using a Nanoscope VIII Multimode AFM (Bruker). Triangular AFM cantilevers (MSCT, Bruker) with silicon nitride tips and a nominal spring constant between 0.01-0.06 N m^{-1} were used. Cantilevers were calibrated at the end of each experiment using the thermal noise method (*53*). Functionalized tips were derivatized using a NHS-PEG_{27}-Malemide linker following a protocol described elsewhere (*54*) to covalently attach the Pep7b linking the cysteine residue added at the C-terminus. After functionalization, the cantilevers were washed with PBS (3 x 5 min) and stored in individual wells of a multiwell dish containing 2 ml of PBS per well at 4°C until used in AFM experiments. Force-distance curves were recorded as 32x32 pixels arrays over 1 x 1 μm^2 areas, using an applied force of 250 pN, a contact time of 0.25 s and a constant approach and retraction speed of 1 µm s^{-1}. For dynamic force spectroscopy measurements, the retraction speed of the cantilever was varied as follows: 20 nm s^{-1}, 100 nm s^{-1}, 200 nm s^{-1}, 1 µm s^{-1}, 2 µm s^{-1}, 10 µm s^{-1} and 20 µm s^{-1}. Typically, at least 2000 force-distance curves were performed for each cantilever at a particular retraction speed. The collected data were analyzed using the Nanoscope Analysis software (Bruker). The retraction segment of each curve was analyzed and unbinding events were considered as specific if they occurred at a distance between 5-50 nm from the contact point. The minimum adhesion force was further used to calculate binding probabilities and build force distribution histograms. To reconstruct the energy landscape of the measured interactions, loading rates were calculated from the force vs time curve, as the slope of the adhesion event before the tip cantilever jumps off to surface. The dependency of the force with the loading rate was then plotted in dynamic force spectroscopy plots.

Statistical analysis

Statistical analysis was performed using GraphPad software. Data represent mean ± SD. p-values were calculated by the one-way ANOVA (post hoc Dunnett's test) and Student's t test for multiple and single comparisons of normally distributed data (STF and PLA assays) and by the Kruskal–Wallis (post hoc Dunn's test) for multiple comparisons of non-normally distributed data (CtA quantifications); *$p<0.05$; **$p<0.01$; ***$p<0.001$.

References

1. C. Y. Logan, R. Nusse, *Annu. Rev. Cell Dev. Biol.* **20**, 781-810 (2004).
2. R. Nusse, H. E. Varmus, *Cell.* **69**, 1073-1087 (1992).
3. P. Bhanot et al., *Nature.* **382**, 225-230 (1996).
4. C. Niehrs, *Nat. Rev. Mol. Cell. Biol*. **13**, 767-779 (2012).
5. B.T. MacDonald, X. He, *Cold Spring Harb. Perspect. Biol.* **4**, doi: 10.1101/cshperspect.a007880 (2012).
6. J. C. Hsieh, A. Rattner, P. M. Smallwood, J. Nathans, *Proc. Natl. Acad. Sci. U. S. A.* **96**, 3546-3551 (1999).
7. A. Kikuchi, H. Yamamoto, S. Kishida, *Cell. Signal.* **19**, 659-671 (2007).
8. C. Wu, R. Nusse, *J. Biol. Chem.* **277**, 41762-41769 (2002).
9. E. J. Rulifson, C. H. Wu, R. Nusse, *Mol. Cell.* **6**, 117-126 (2000).
10. S. L. Holmen, A. Salic, C. R. Zylstra, M. W. Kirschner, B. O. Williams, *J. Biol. Chem.* **277**, 34727-34735 (2002).
11. H. Yu, X. Ye, N. Guo, J. Nathans, *Development.* **4394**, 4383-4394 (2012).
12. Y. K. Wang et al., *Hum. Mol. Genet.* **6**, 465-72 (1997).
13. C. Y. Janda, D. Waghray, A. M. Levin, C. Thomas, K. C. Garcia, *Science*. **337**, 59-64 (2012).
14. J. M. Stenman et al., *Science*. **322**, 1247-1250 (2008).
15. R. Daneman et al., *Proc. Natl. Acad. Sci. U. S. A.* **106**, 641-646 (2009).
16. S. Liebner et al., *J. Cell Biol.* **183**, 409-417 (2008).
17. M. Cullen et al., *Proc. Natl. Acad. Sci. U. S. A.* **108**, 5759-5764 (2011).
18. F. Kuhnert et al., *Science*. **330**, 985-989 (2010).
19. K. D. Anderson et al., *Proc. Natl. Acad. Sci. U. S. A.* **108**, 2807-2812 (2011).
20. Y. Zhou, J. Nathans, *Dev. Cell.* **31**, 248-256 (2014).
21. E. Posokhova et al., *Cell Rep.* **10**, 123-130 (2015).
22. B. Vanhollebeke et al., *Elife*. **4**, 1-25 (2015).
23. F. Ulrich et al., *Development.* **143**, 147-159 (2015).
24. C. Cho, P. M. Smallwood, J. Nathans, *Neuron*. ***95***, 1056-1073 (2017).
25. F. A. Ran et al., *Nat. Protoc.* **8**, 2281-2308 (2013).

26. P.E. Wright, H. J. Dyson, *Nat. Rev. Mol. Cell. Biol.* **16**, 18-29 (2015).

27. M. L. H. Chu et al., *Structure*. **21**, 1235-1242 (2013).

28. R. W. Friddle, A. Noy, J. J. De Yoreo, *Proc. Natl. Acad. Sci.* **109**, 13573-13578 (2012).

29. N. Bostaille, A. Gauquier, L. Twyffels, B. Vanhollebeke, *Biol. Open*. **5**, 1874-1881 (2016).

30. S. Harmansa, I. Alborelli, D. Bieli, E. Caussinus, M. Affolter, *Elife*. **6**, 1-22 (2017).

31. X. Li et al., *Development*. **140**, 3028-3039 (2013).

32. S. I. Yanagawa, F. Van Leeuwen, A. Wodarz, J. Klingensmith, R. Nusse, *Genes Dev.* **9**, 1087-1095 (1995).

33. X. Huang et al., *Science.* **339**, 1441-1445 (2013).

34. M. Gammons, M. Bienz, *Curr. Opin. Cell Biol.* **51**, 42-49 (2018).

35. M. Bienz, *Trends Biochem. Sci.* **39**, 487-495 (2014).

36. J. Bilic et al., *Science.* **316**, 1619–1622 (2007).

37. M. V. Gammons, M. Renko, C. M. Johnson, T. J. Rutherford, M. Bienz, *Mol. Cell.* **64**, 92-104 (2016).

38. M. B. Lai et al., *Cell Rep*. **19**, 2809-2822 (2017).

39. Z. F. Zimmerman, R. T. Moon, A. J. Chien, *Cold Spring Harb. Perspect. Biol.* **4** (2012), doi:10.1101/cshperspect.a008086.

40. A. Koval, V. L. Katanaev, *Drug Discov. Today.* **17**, 1316-1322 (2012).

41. H. Clevers, R. Nusse, *Cell.* **149**, 1192-1205 (2012).

42. E. Driehuis, H. Clevers, *Br. J. Pharmacol.* **174**, 4547-4563 (2017).

43. J. Chang et al., *Nat. Med.* **23**, 450-460 (2017).

44. C. B. Kimmel, W. W. Ballard, S. R. Kimmel, B. Ullmann, T. F. Schilling, *Dev. Dyn.* **203**, 253-310 (1995).

45. S. W. Jin, D. Beis, T. Mitchell, J. N. Chen, D. Y. R. Stainier, *Development.* **132**, 5199-5209 (2005).

46. N. C. Chi et al., *Genes Dev.* **22**, 734-739 (2008).

47. L. E. Jao, S.R. Wente, W. Chen, *Proc. Natl. Acad. Sci.* **110**, 13904-13909 (2013).

48. E. S. Weinberg et al., *Development.* **122**, 271-280 (1996).

49. C. Thisse, B. Thisse, *Nat. Protoc.* **3**, 59-69 (2008).

50. B. T. MacDonald et al., *J.Biol. Chem.* **289**, 18122-18136 (2014).

51. B. Webb, A. Sali, *Current Protocols in Bioinformatics* (John Wiley & Sons, Inc., Hoboken, NJ, USA, 2016), vol. 54, p. 5.6.1-5.6.37.

52. J. C. Phillips et al., *J. Comput. Chem.* **26**, 1781-1802 (2005).

53. H. J. Butt, M. Jaschke, *Nanotechnology*. **6**, 1-7 (1995).

54. L. Wildling et al., *J. Biol. Chem.* **287**, 105-113 (2012).

Figure legends

Figure 1. Reck is a Frizzled-independent Wnt7-specific receptor

(A) Schematics of the Wnt7 receptor complex components and strategy for their genetic inactivation. Cells transfected with a bicistronic construct encoding the sgRNA and SpCas9-2A-GFP were iteratively cloned by FACS *(25)*. (B) Anti-V5 immunostaining of transiently-expressed Wnt7a-V5 or Wnt3a-V5 in cells of the indicated genotype. (C) Same as (B) for cells transiently co-expressing Wnt7a-V5 and the indicated (co)-receptors. (D) Proximity ligation assay (PLA) using anti-V5 and anti-HA antibodies directed against Wnt7a-V5 and the indicated HA-tagged (co)-receptors expressed in *GPR124*$^{-/-}$*;RECK*$^{-/-}$ cells. Signal quantification is on the right (see Methods). (E) Anti-V5/HA PLAs between the indicated V5-tagged Wnt ligand and HA-Reck in *GPR124*$^{-/-}$*;RECK*$^{-/-}$ cells. (F) Anti-V5/HA PLAs in (1:1) co-cultures of Wnt7a-V5 or Wnt3a-V5 secreting WT cells and *FZ*$_{1\text{-}10}^{-/-}$ HEK293T cells co-expressing HA-Reck and cytosolic GFP as a transfection marker. (G) Ligand capture assay in triple (1:1:1) co-cultures. Luciferase activities of HEK293-STF reporter cells transfected with Fz5 (yellow cell) and stimulated in a paracrine manner by co-cultured Wnt7a or Wnt3a secreting cells in the presence of *FZ*$_{1\text{-}10}^{-/-}$ HEK293T competing cells transfected with various (co)-receptors as indicated. Scale bars, 10 μm. $^{***}p<0.001$, data represent mean ± SD.

Figure 2. Wnt7 recognition involves its intrinsically disordered linker region

(A) Anti-V5/HA PLAs between Wnt7a-V5 and HA-Reck or its variants co-expressed in *GPR124*$^{-/-}$*;RECK*$^{-/-}$ cells in the absence of Gpr124. Quantification is shown on the right. (B) Quantification as in (A) in the presence of Gpr124. (C) Reck and its Gpr124 and Wnt7 binding partners. (D) Structural modeling of Wnt7a based on the crystal coordinates of XWnt8a. The N-terminal domain (NTD) and C-terminal domain (CTD) are pseudo-colored in cyan and grey, respectively. The NTD-embedded linker region is circled in purple. (E) Schematic representation of the V5-tagged Wnt variants examined in the anti-V5/HA PLAs shown and quantified in (F) in *GPR124*$^{-/-}$*;RECK*$^{-/-}$ cells co-expressing HA-Reck. (G) Gpr124/Reck-dependent luciferase activities of 101 different single-residue variants of Wnt7a normalized to WT Wnt7a in HEK293-STF cells. (H) Alignment of the Wnt7 linker domain across the vertebrate clade. Mm, *Mus musculus*; Gg, *Gallus gallus*; Xl, *Xenopus laevis*; Dr, *Danio rerio.* The residues of Mm Wnt7a are color-coded according to their activity class determined in (G). (I) Anti-V5/HA PLAs between Wnt7a-V5 or Wnt7a^{4A}-V5 and HA-Reck. Ligand secretion was evaluated by semi-quantitative anti-V5 dot blot analysis of serially diluted cell supernatant. Scale bars, 10 μm. $^{*}p<0.05$, $^{***}p<0.001$, data represent mean ± SD.

Figure 3. The Wnt7 linker peptide binds the Reck CK domain with low micromolar affinity

(A) Coomassie Blue staining of the recombinant Reck-CK-Fc fusion proteins used in biophysical analyses. (B) Interaction between Reck-CK-Fc and synthetic pWnt7 peptides using isothermal titration calorimetry (ITC). ITC of pWnt7a, pWnt7a^{4A} and pWnt3a into Reck-CK-Fc (upper pannels). ITC of Reck-CK-Fc and its CK motif variants to pWnt7b (middle and bottom panels). (C) Probing Reck-CK-Fc/pWnt7b interaction using single molecule force spectroscopy (SMFS). Principle of force-distance curve based atomic force microscopy (FD-based AFM). An AFM tip functionalized with a PEG spacer fused to the pWnt7b peptide is approached and retracted from a surface coated with Reck-CK-Fc. (D) Force-time curve from which the loading rate (LR) can be extracted from the slope of the curve just before bond rupture ($LR=\Delta F/\Delta t$). (E) Force-distance curves recorded at various retraction speeds (from 20 nm s^{-1} to 20 μm s^{-1}) and showing no adhesion event (first curve) or specific adhesion events (other curves). (F) Loading rate-dependent interaction forces of single Wnt7 ligand-receptor bonds quantitate the ligand-binding energy landscape of Reck. Fitting the data using the Friddle-Noy-de Yoreo model (thin red line) *(28)* provides average F_{eq}, x_u, ΔG_{bu}, k^0_u and K_D with errors representing the S.E. (inset). Each circle represents one measurement. Darker shaded areas represent 95% prediction interval.

Figure 4. Gpr124 function in Wnt signaling does not depend on its GPCR structure

(A) Potential Wnt7-specific signal transduction mechanisms. (B) Luciferase activity (left) and anti-V5 immunostaining (right) of HEK293-STF cells co-transfected with Fz5, Wnt7a and the indicated (co)-receptors. (C) Experimental setup for *in vivo* brain angiogenesis assays in zebrafish embryos after RNA injections at the one-cell stage. The red area is imaged to analyze the hindbrain central arteries (CtAs). (D) Gpr124 and its domain variants. (E) Representative 3D wire diagrams of the 60 hpf cerebrovasculature of WT and *gpr124* mutant embryos injected with 100 pg of the indicated RNA. Red vessels represent the Gpr124/Reck-dependent intracerebral CtAs that sprout from the grey perineural primordial hindbrain channels (PHBCs); see Fig. S13 for the confocal stacks used to generate the wire diagrams. (F) Hindbrain CtAs of 60 hpf *gpr124* morphant embryos injected at the one-cell stage with 100 pg of the indicated mRNA. (G) Bimolecular GPCR complementation assay strategy. Membrane receptors (Gpr124, Gpr125 and $Gpr124^{ECD}$-TM^{CD27}) inactivated by ICD/GFP substitutions are co-expressed with VhhGFP4 fusions to reconstitute a bimolecular adduct through an artificial GFP-VhhGFP4 linker. (H) Hindbrain CtAs of 60 hpf *gpr124* morphant embryos injected at the one-cell stage with 100 pg of the indicated mRNAs. (I) Gpr124 and its essential protein interactions. Scale bar, 10 μm. $^{**}P<0.01$, $^{***}P<0.001$; data represent mean ± SD.

Figure 5. Gpr124 interacts with Dvl through its ICD

(A) Hindbrain CtAs of 60 hpf *gpr124* morphant embryos injected at the one-cell stage with 100 pg mRNA encoding the illustrated receptors. (B) WISH of *myod1* expression at the 7-somite stage embryos, control or injected with 250 pg of *gpr125* or *gpr124* mRNA. The red lines indicate the mediolateral broadening of the AP axis. (C) Intracellular distribution of Gpr124-tagRFP and Dvl-GFP expressed individually in zebrafish blastulae. (D) Intracellular distribution of Gpr124-tagRFP and Dvl-GFP co-expressed in zebrafish blastulae. The cells annotated with an asterisk are magnified in the right panels and the pixel intensity of the green and red channels along a virtual clockwise path following the cell cortex from a to b is plotted below. In (C) and (D), open and filled arrowheads point respectively to Gpr124-negative and Gpr124-positive membrane microdomains in EVL and DEL cells. (E) Gpr124 and its ICD variants. (F) Luciferase dose response values of HEK293-STF cells co-transfected with Wnt7a, Fz1, Reck and increasing amounts of Gpr124 constructs or its ICD variants as illustrated in (E). (G) Hindbrain CtAs of 60 hpf *gpr124* morphant embryos injected at the one-cell stage with 100 pg of the indicated mRNA. (H) Intracellular distribution of Dvl-GFP co-expressed with Gpr124 and its ICD variants in zebrafish blastula EVL cells. (I) same as (H) in $FZ_{1\text{-}10}^{-/-}$ cells. In (H) and (I), red arrowheads point to Dvl-GFP signal at the plasma membrane. (J) Anti-FLAG co-immunoprecipitation assays in total lysates of cells co-expressing Dvl-GFP and N-terminal FLAG-tagged versions of Gpr124 or its ICD variants. (K) Mosaic gene disruption in F_0 zebrafish embryos by injection at the one cell-stage of 150 pg of *zCas9* mRNA and 50 pg of the illustrated sgRNAs. Resulting hindbrain vasculature scored at 48 hpf. BA, Basilar artery. Scale bars, 10 μm. $^{**}P<0.01$, $^{***}P<0.001$; data represent mean ± SD.

Figure 6. Dvl polymers assemble ligand-specific Wnt signalosomes by linking Fz and Gpr124

(A) Hindbrain CtAs of 60 hpf WT or *gpr124* morphant embryos injected at the one-cell stage with 50 pg of the indicated mRNA. Of note, the injected doses of mRNA were reduced compared to Fig. 4H to avoid the developmental toxicity of *VhhGFP4-Dvl* mRNA injections. Representative hindbrain vasculature shown on the right. (B) Intracellular distribution of Fz4-GFP and Gpr124-tagRFP expressed individually or in the presence of Dvl in zebrafish blastula DEL cells. (C) Intracellular distribution of Dvl-GFP co-expressed with Fz4 or Gpr124 in zebrafish blastula DEL cells. (D) Intracellular distribution of co-expressed Fz4-GFP and Gpr124-tagRFP in the absence or presence of Dvl in zebrafish blastula DEL cells. The cells annotated with an asterisk are magnified in the right panels and the pixel intensity of the green and red channels along a virtual clockwise path following the cell cortex from a to b is plotted below. (E) same as (D) in EVL cells. (F) BiFC signals in zebrafish DEL cells expressing Gpr124-VN155 (I152L) and Fz1-VC155 in the presence or absence of Dvl overexpression. (G) Integrated model for Gpr124/Reck-dependent, Wnt7-specific Fz signaling. Refer to the text for details. Scale bars, 10 μm. $^{***}P<0.001$; data represent mean ± SD.

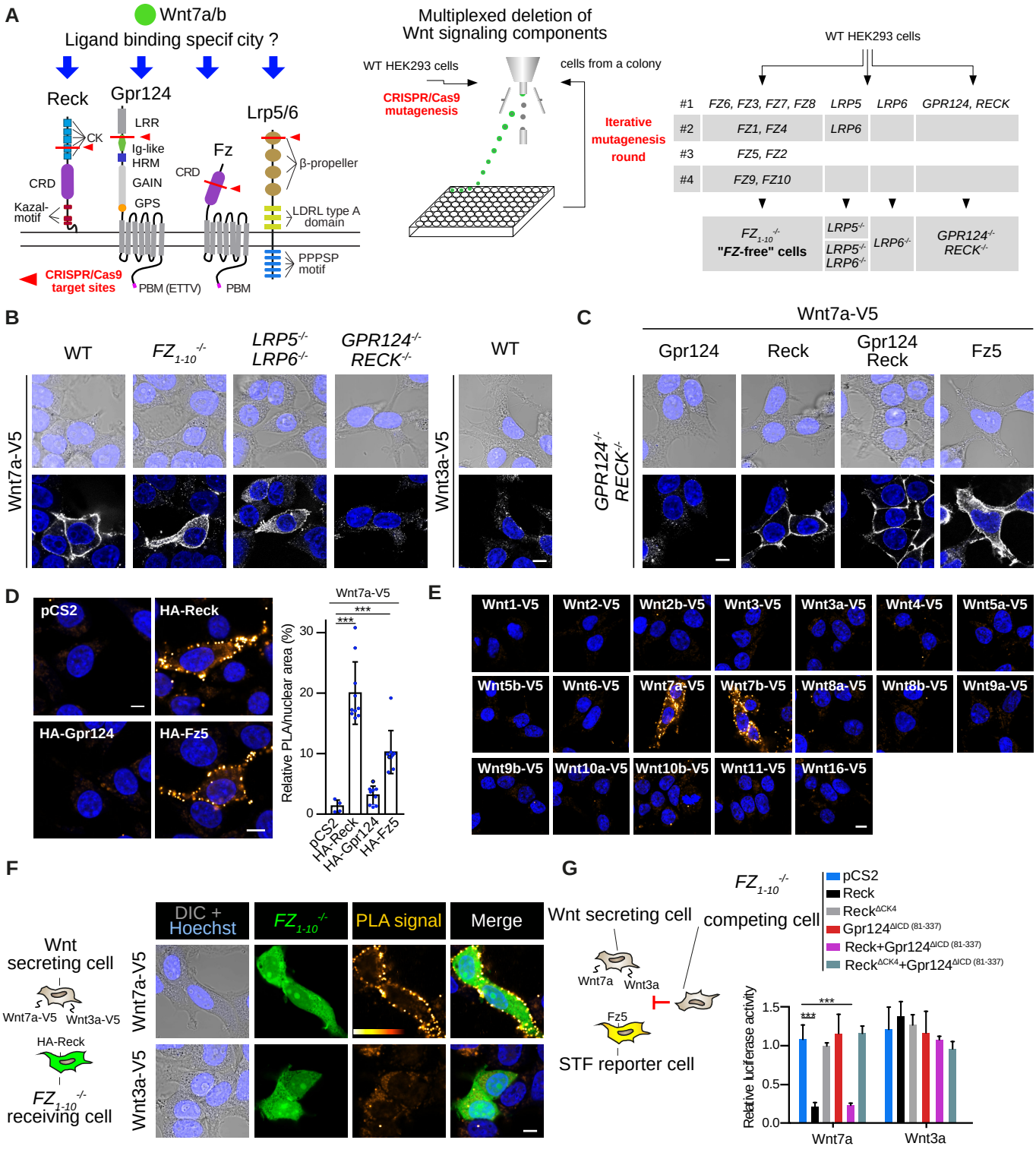

Eubelen et al. Figure 1

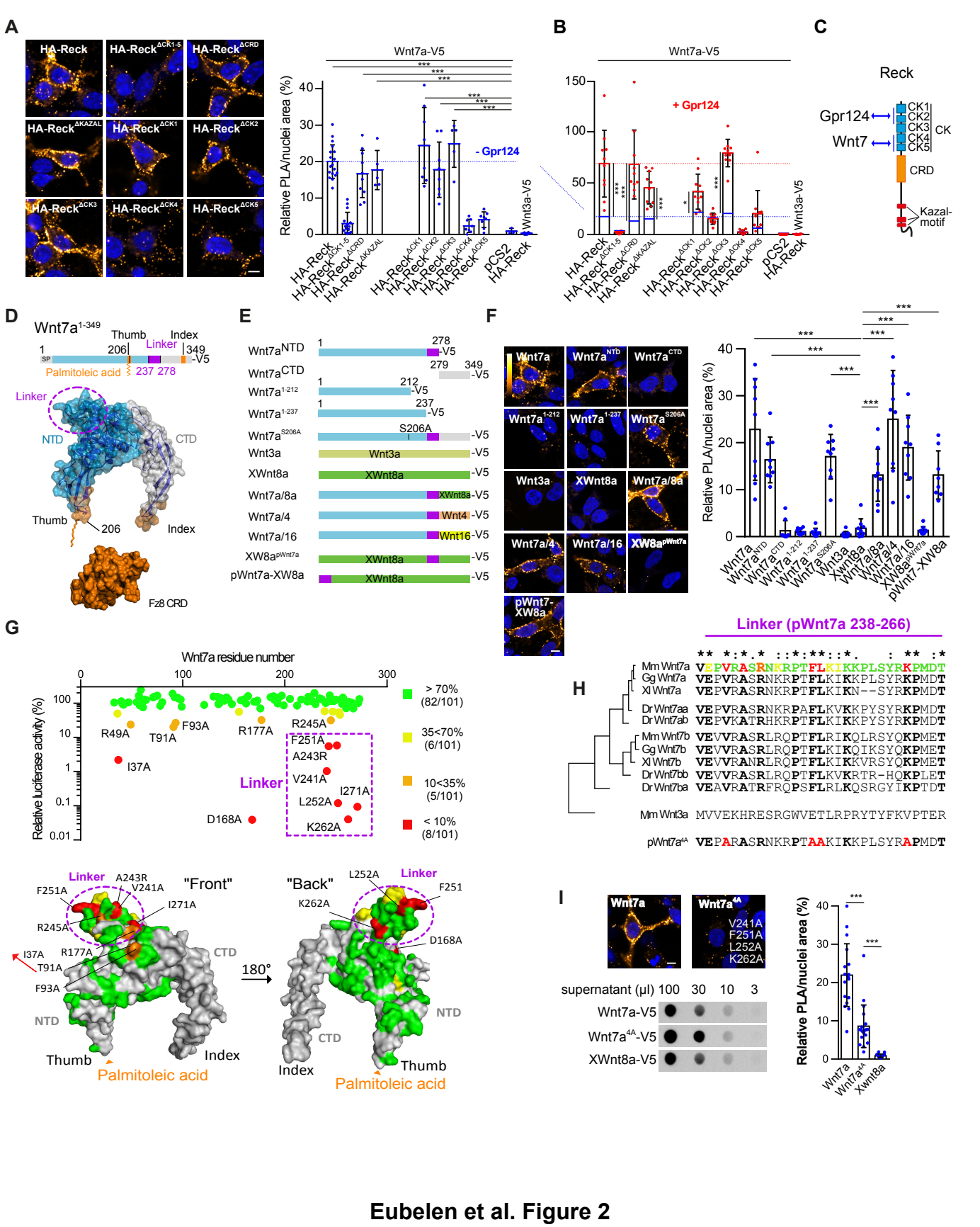

Eubelen et al. Figure 2

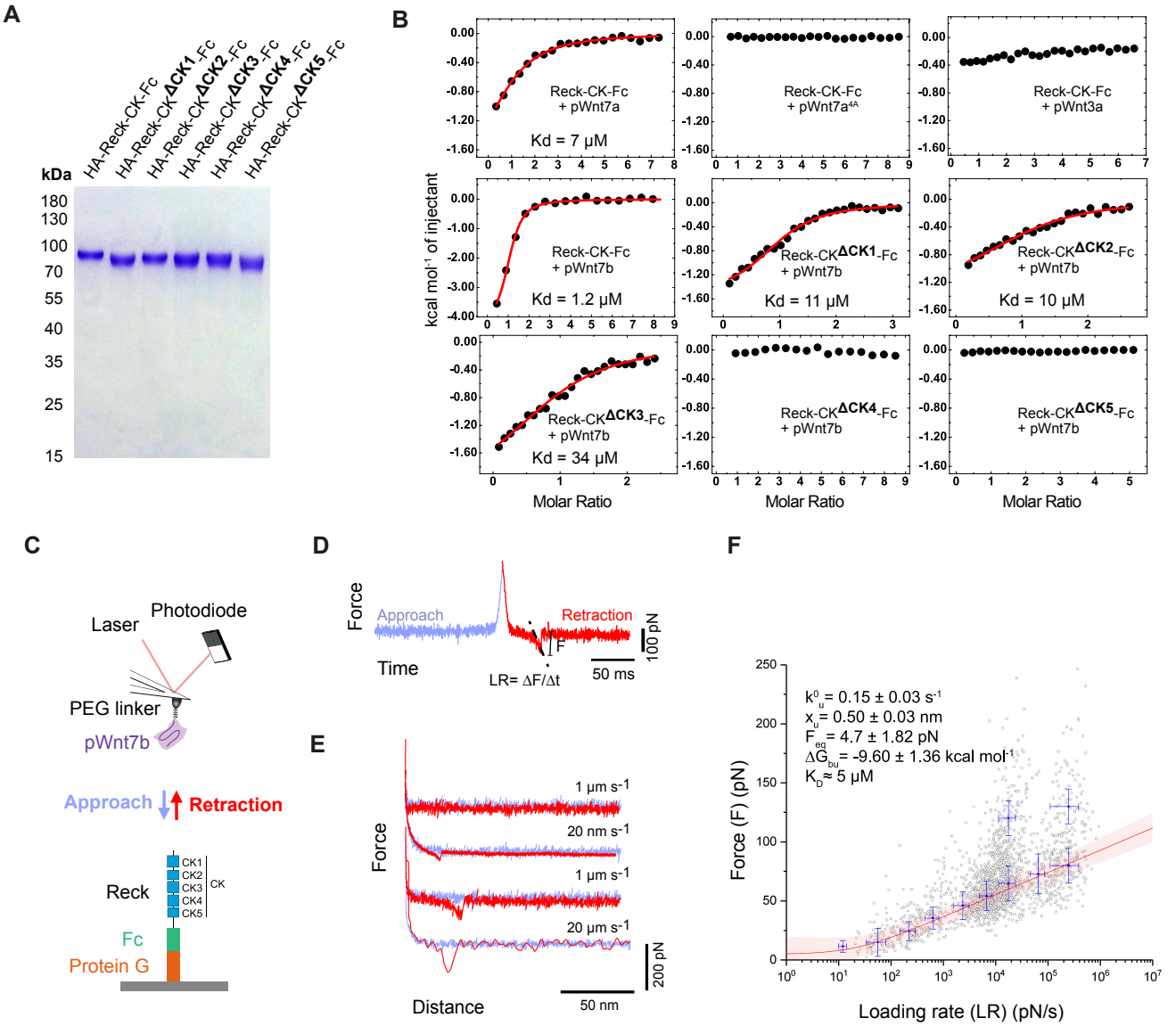

Eubelen et al. Figure 3

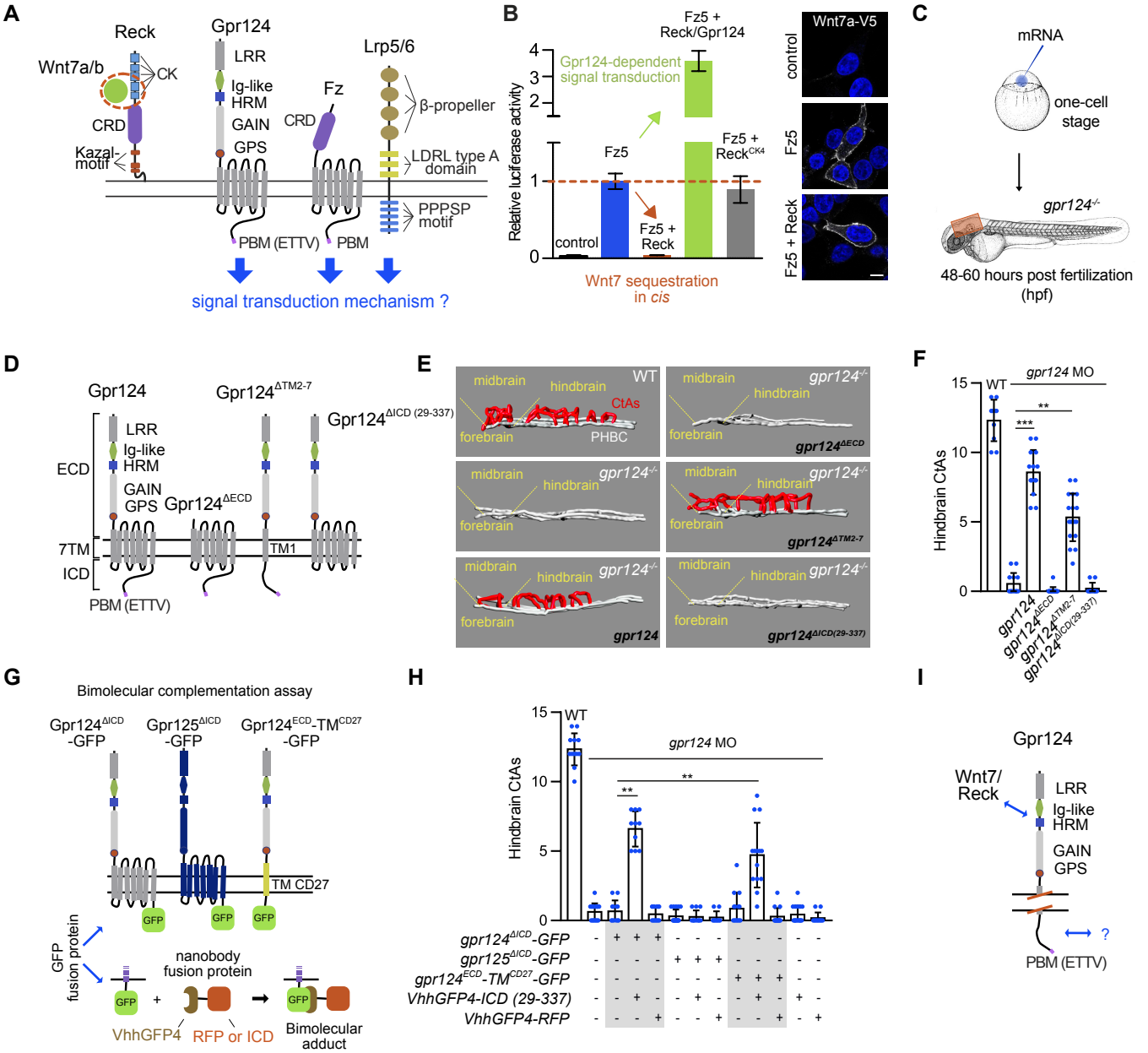

Eubelen et al. Figure 4

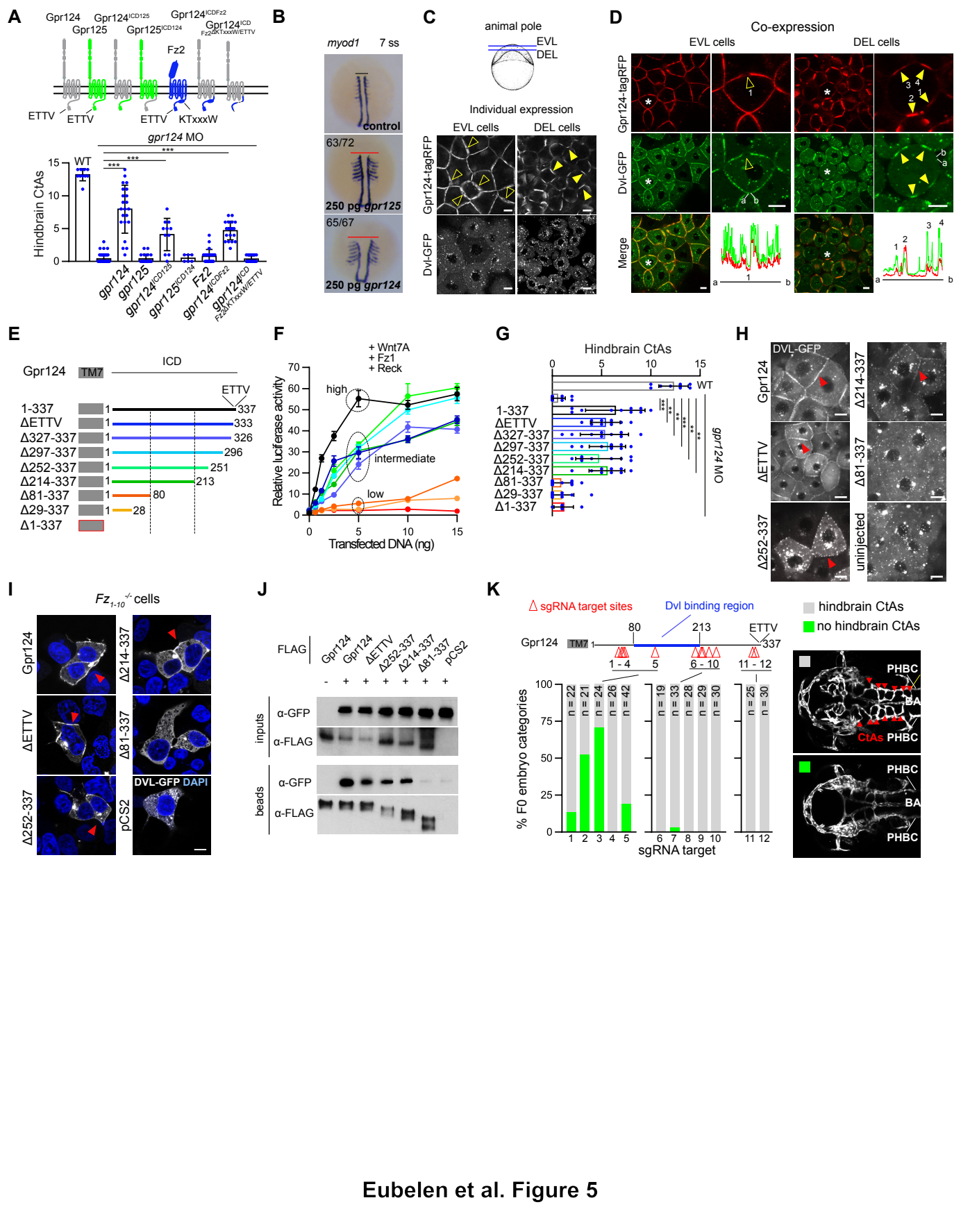

Eubelen et al. Figure 5

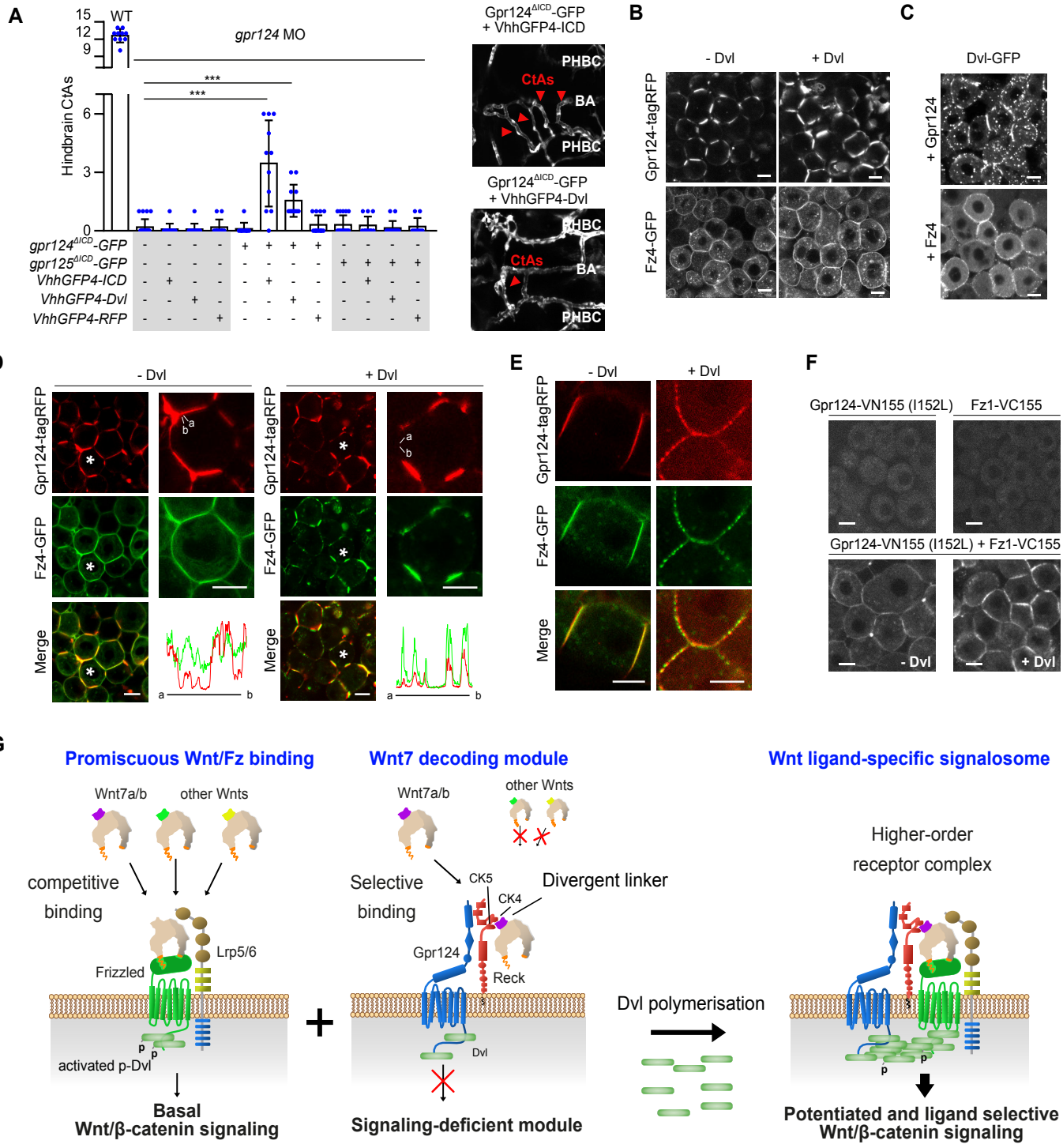

Eubelen et al. Figure 6

Science
AAAS

A molecular mechanism for Wnt ligand-specific signaling

Marie Eubelen, Naguissa Bostaille, Pauline Cabochette, Anne Gauquier, Patricia Tebabi, Andra C. Dumitru, Melanie Koehler, Philipp Gut, David Alsteens, Didier Y.R. Stainier, Abel Garcia-Pino and Benoit Vanhollebeke

Correspondence to: Benoit.Vanhollebeke@ulb.ac.be

This PDF file includes:

Figs. S1 to S22
Tables S1

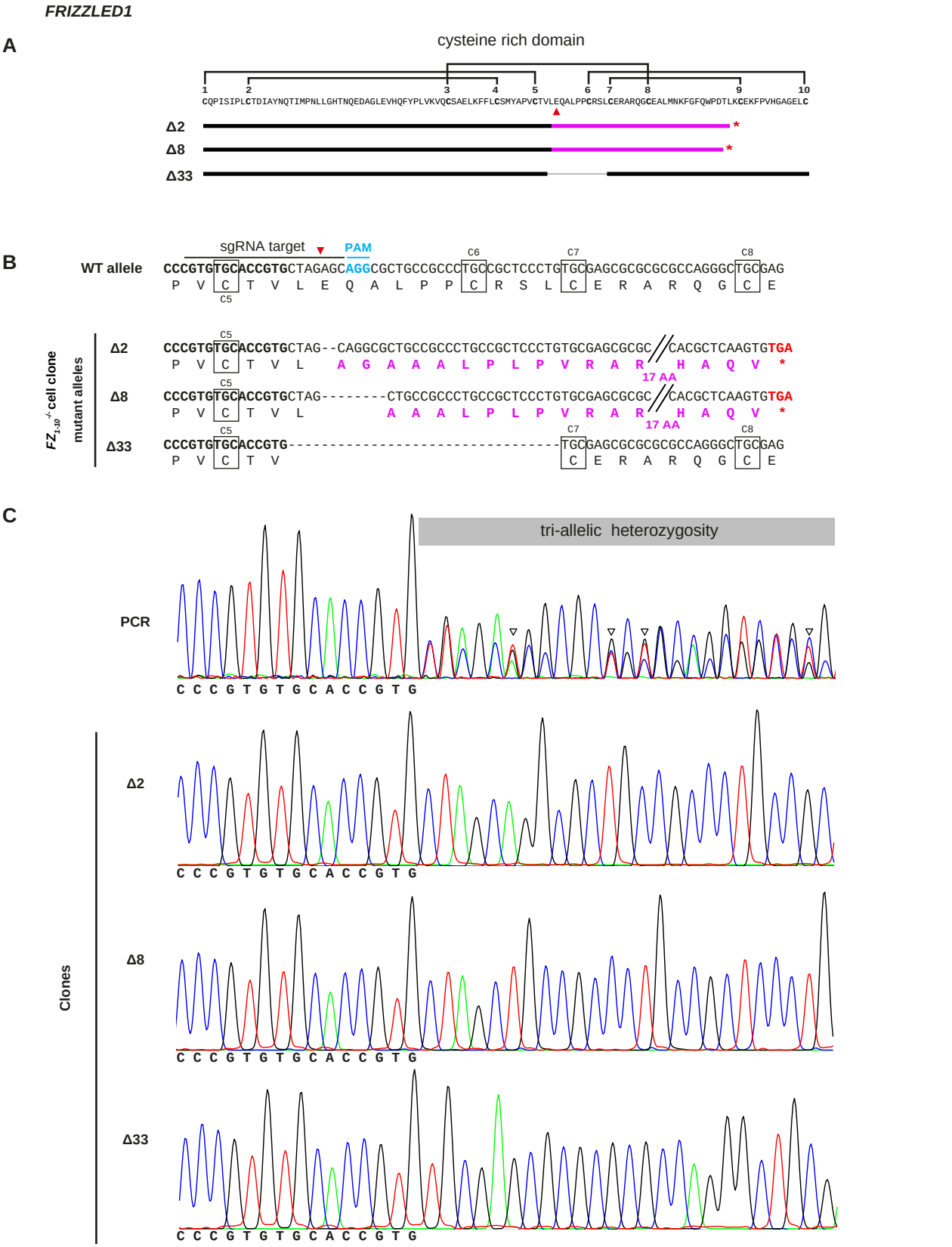
FRIZZLED1
A
cysteine rich domain
1 2 3 4 5 6 7 8 9 10
CQPISIPLCTDIAYNQTIMPNLLGHTNQEDAGLEVHQFYPLVKVQCSAELKFFLCSMYAPVCTVLEQALPPCRSLCERARQGCEALMNKFGFQWPDTLKCEKFPVHGAGELC
Δ2
Δ8
Δ33
B
sgRNA target
PAM
WT allele
CCCGTGTGCACCGTGCTAGAGCAGGCGCTGCCGCCCTGCCGCTCCCTGTGCGAGCGCGCGCCAGGGCTGCGAG
P V C T V L E Q A L P P C R S L C E R A R Q G C E
C5 C6 C7 C8
FZ1-10 -/- cell clone mutant alleles
Δ2
CCCGTGTGCACCGTGCTAG--CAGGCGCTGCCGCCCTGCCGCTCCCTGTGCGAGCGCGC//CACGCTCAAGTGTGA
P V C T V L A G A A A L P L P V R A R H A Q V *
17 AA
Δ8
CCCGTGTGCACCGTGCTAG--------CTGCCGCCCTGCCGCTCCCTGTGCGAGCGCGC//CACGCTCAAGTGTGA
P V C T V L A A A L P L P V R A R H A Q V *
17 AA
Δ33
CCCGTGTGCACCGTG----------TGCGAGCGCGCGCGCCAGGGCTGCGAG
P V C T V C E R A R Q G C E
C
tri-allelic heterozygosity
PCR
C C C G T G T G C A C C G T G
Clones
Δ2
C C C G T G T G C A C C G T G
Δ8
C C C G T G T G C A C C G T G
Δ33
C C C G T G T G C A C C G T G

Fig. S1.

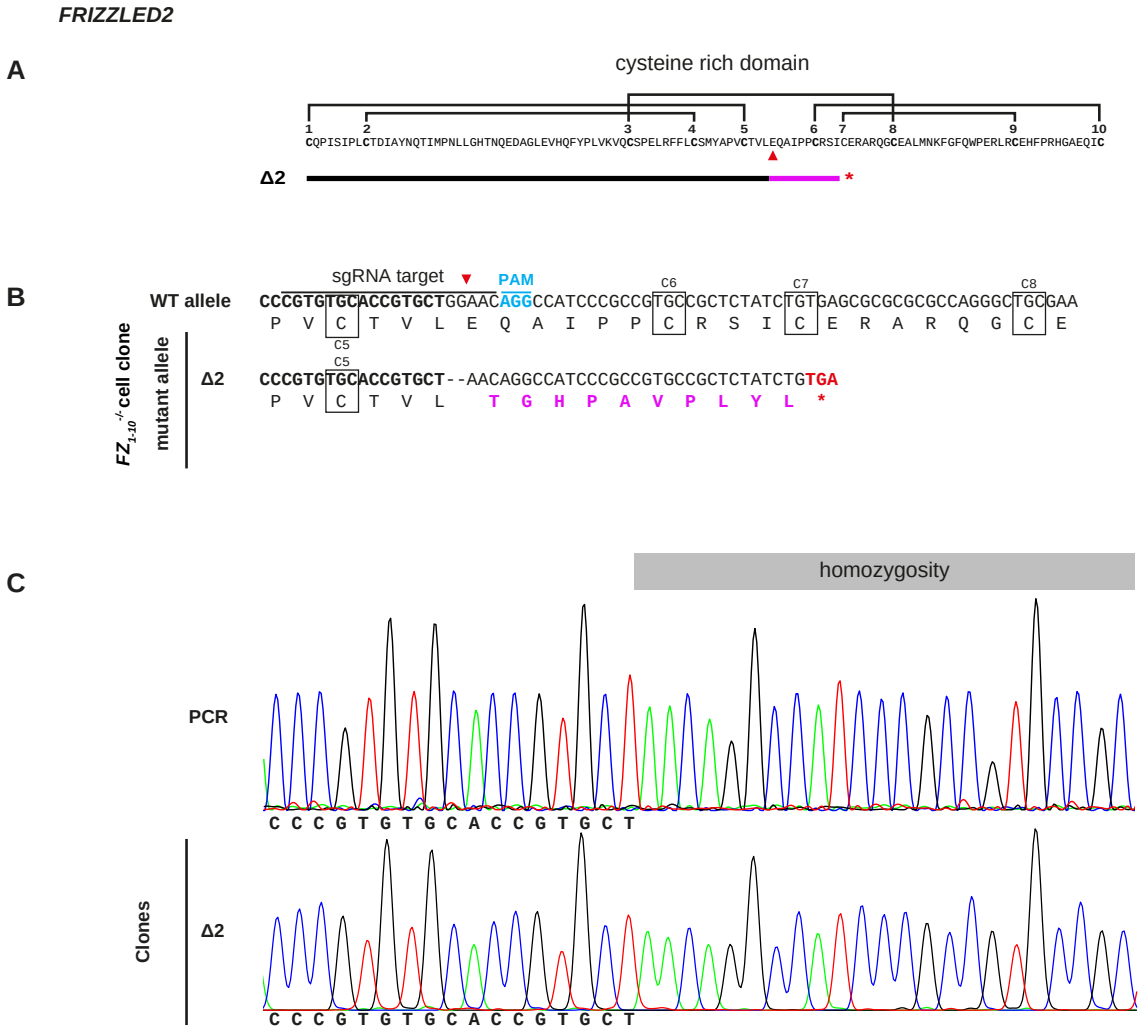

Fig. S1. (continued)

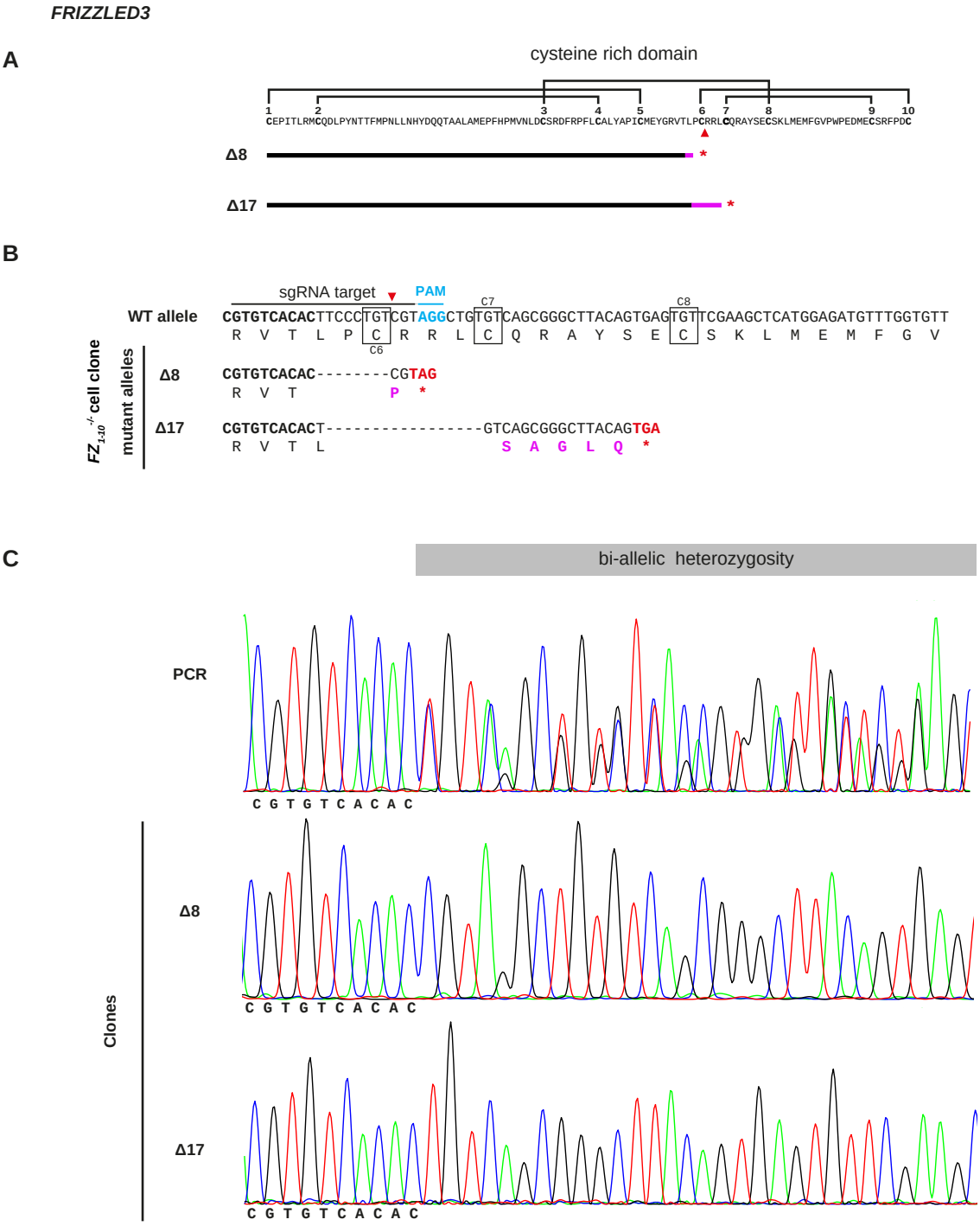

Fig. S1. (continued)

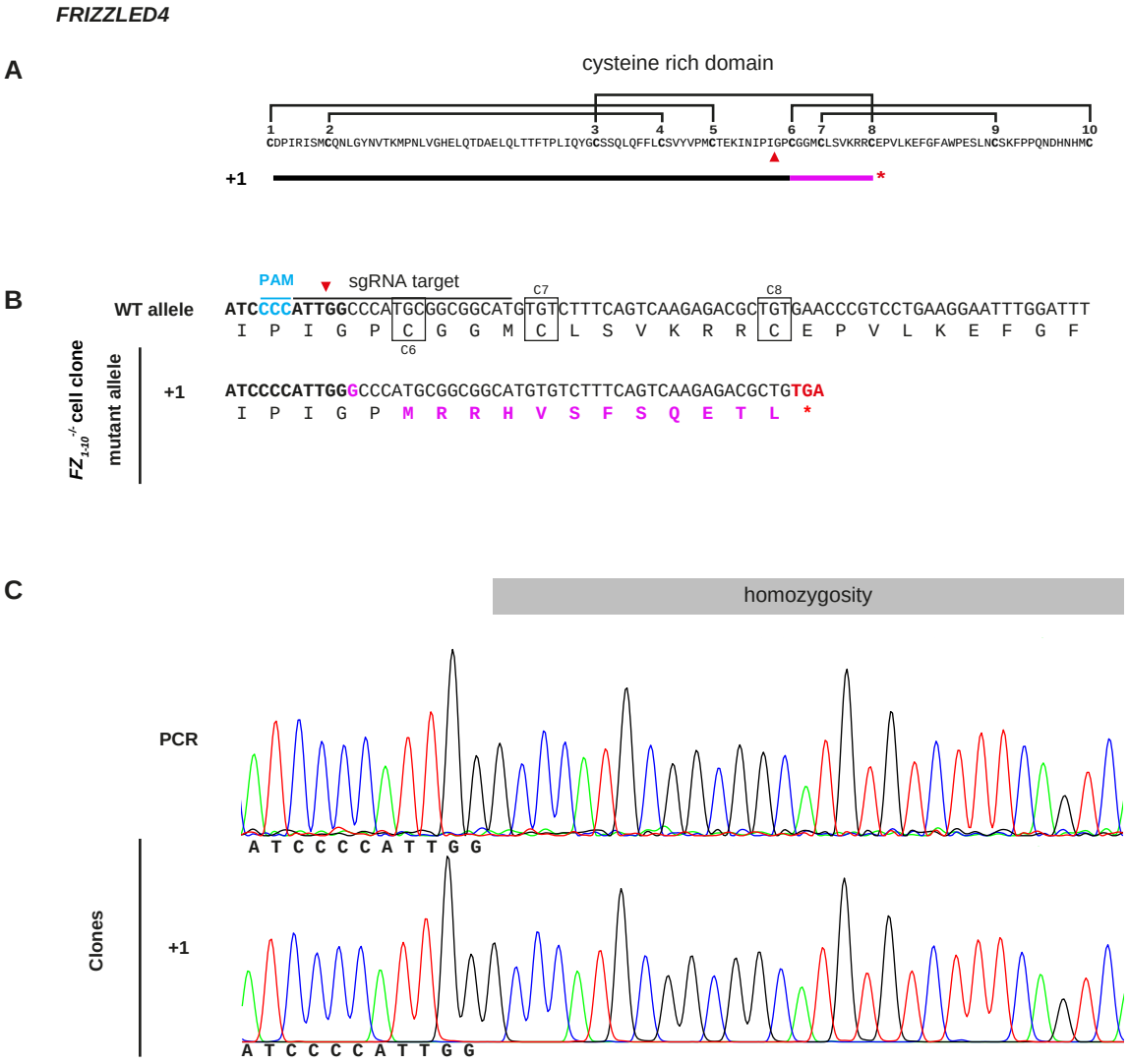

Fig. S1. (continued)

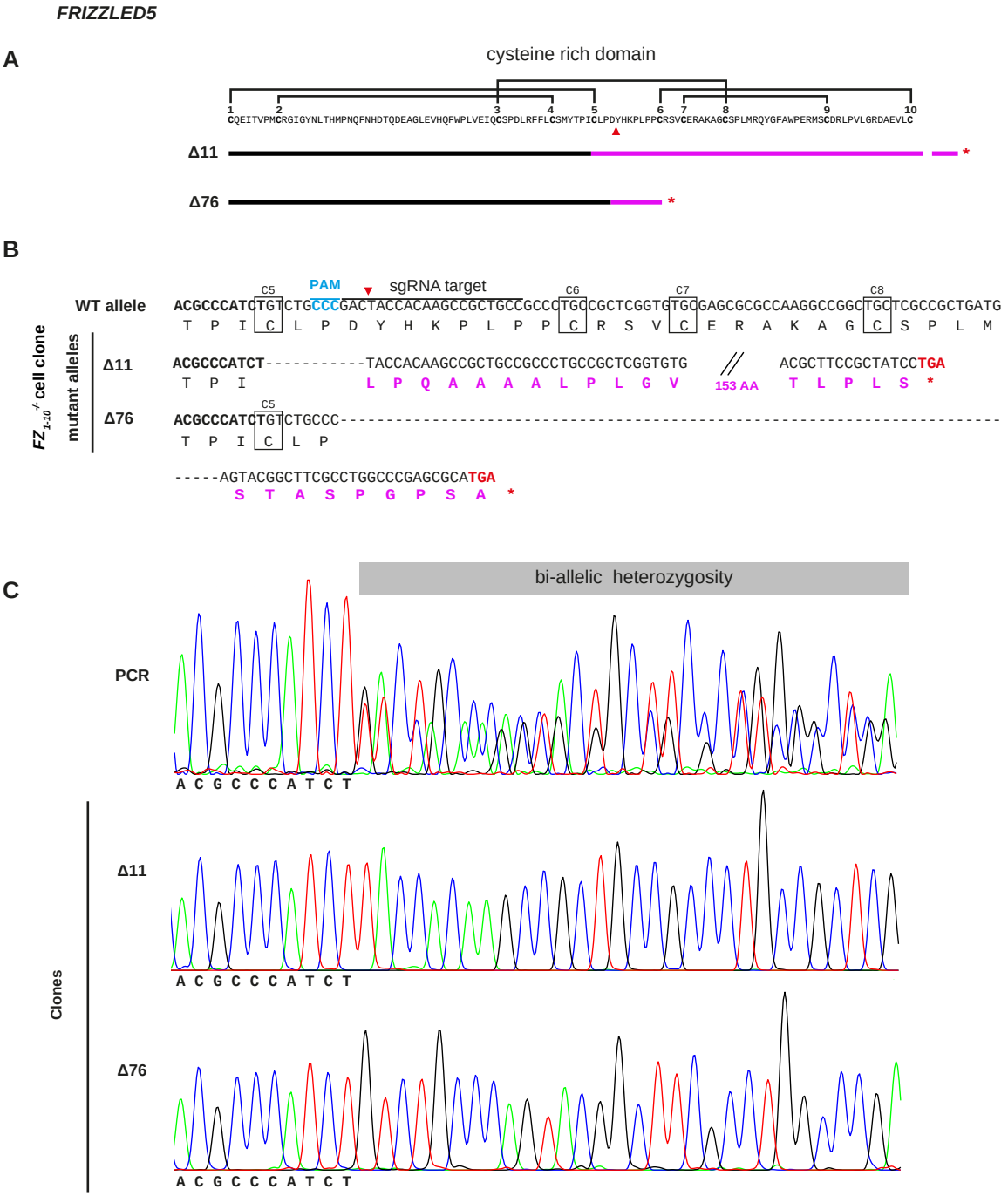

Fig. S1. (continued)

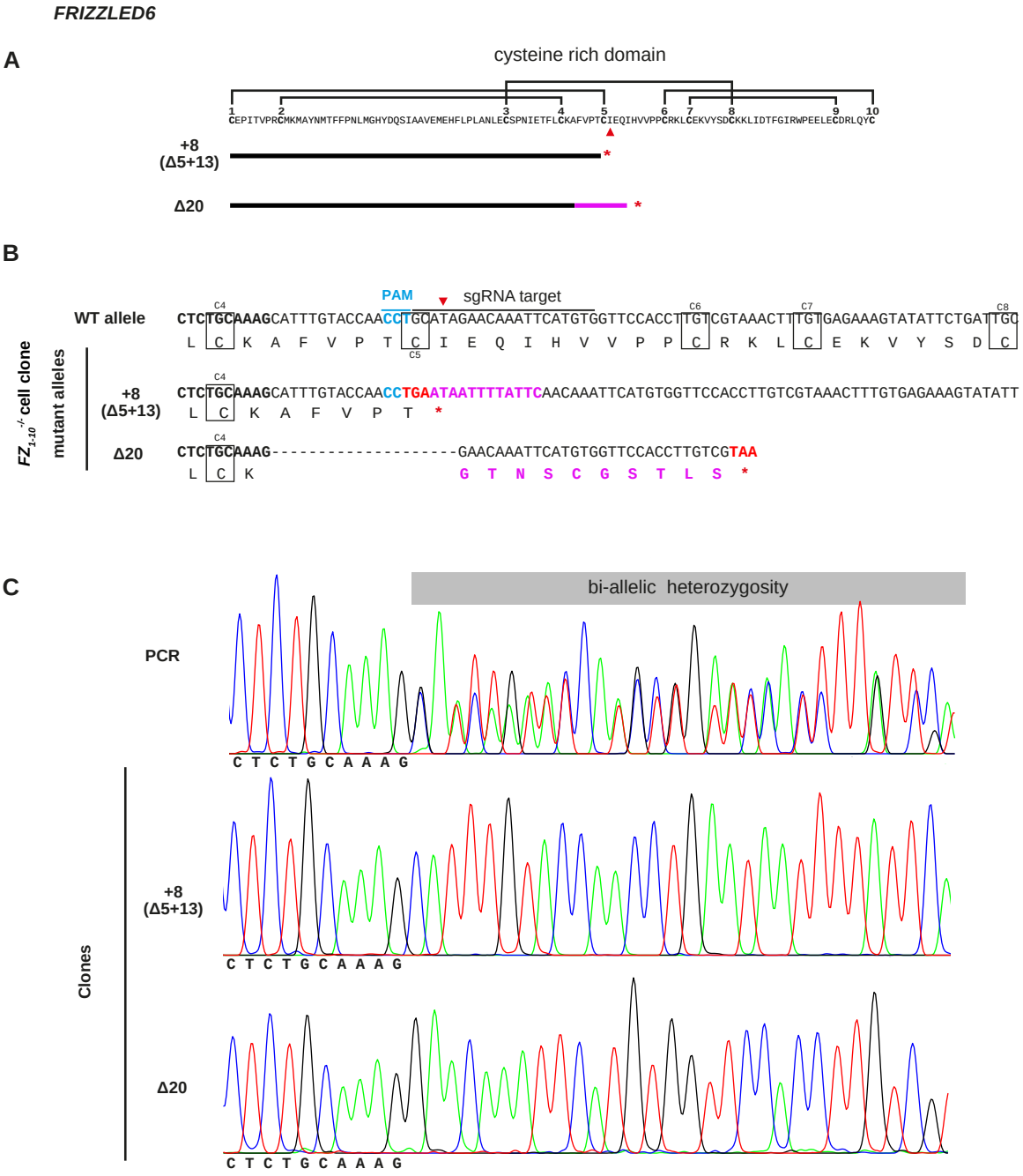

Fig. S1. (continued)

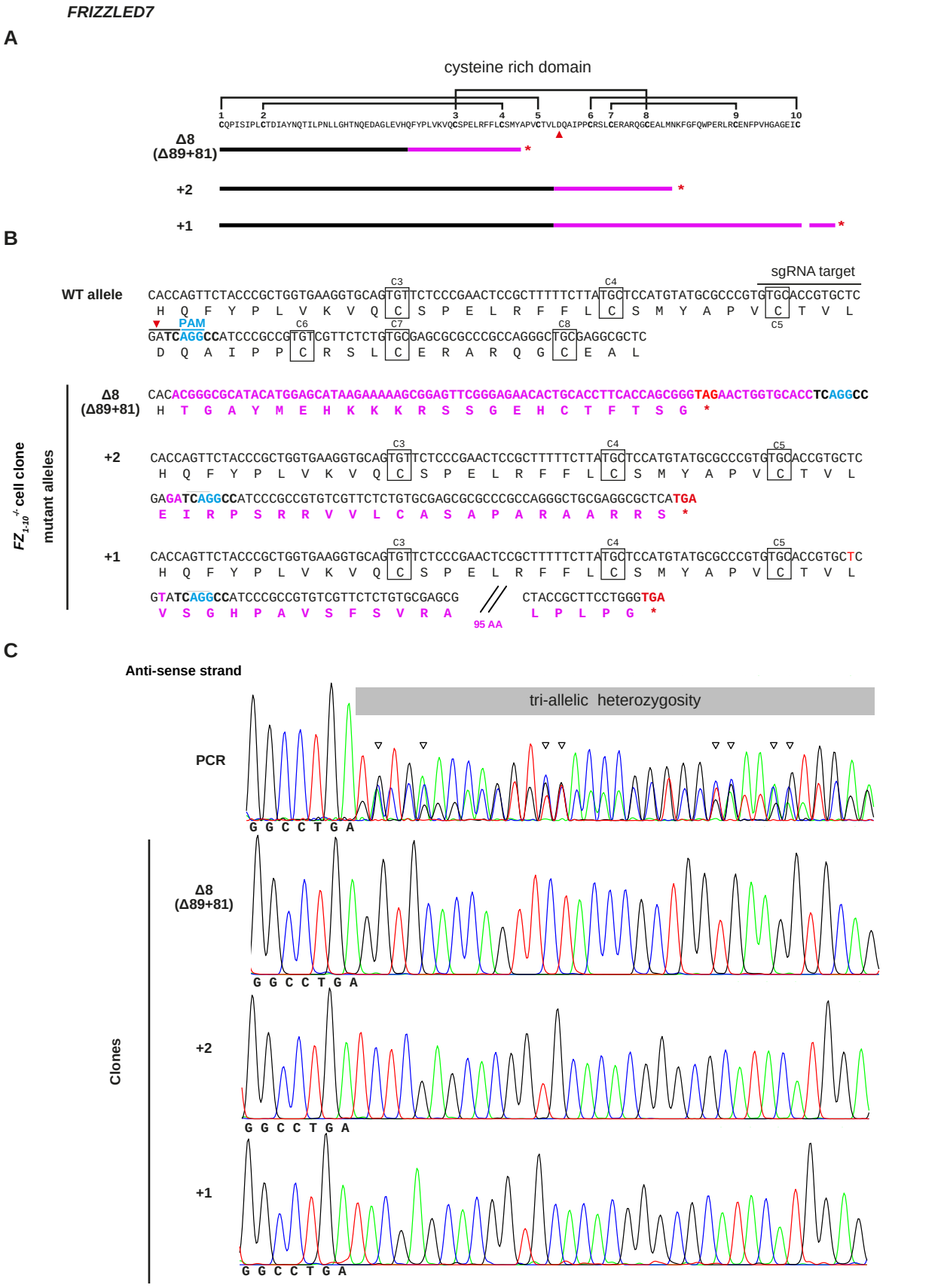

Fig. S1. (continued)

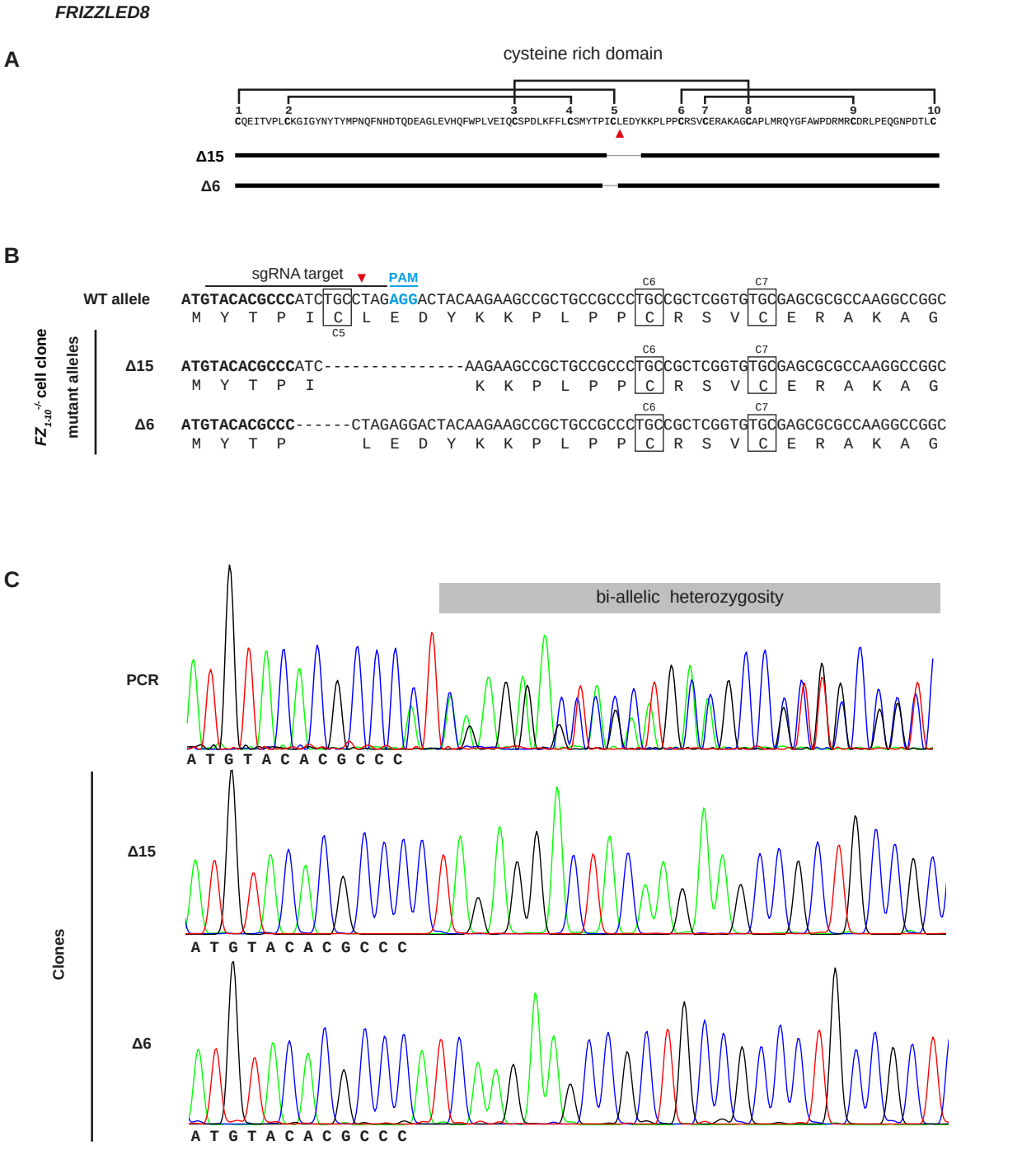

Fig. S1. (continued)

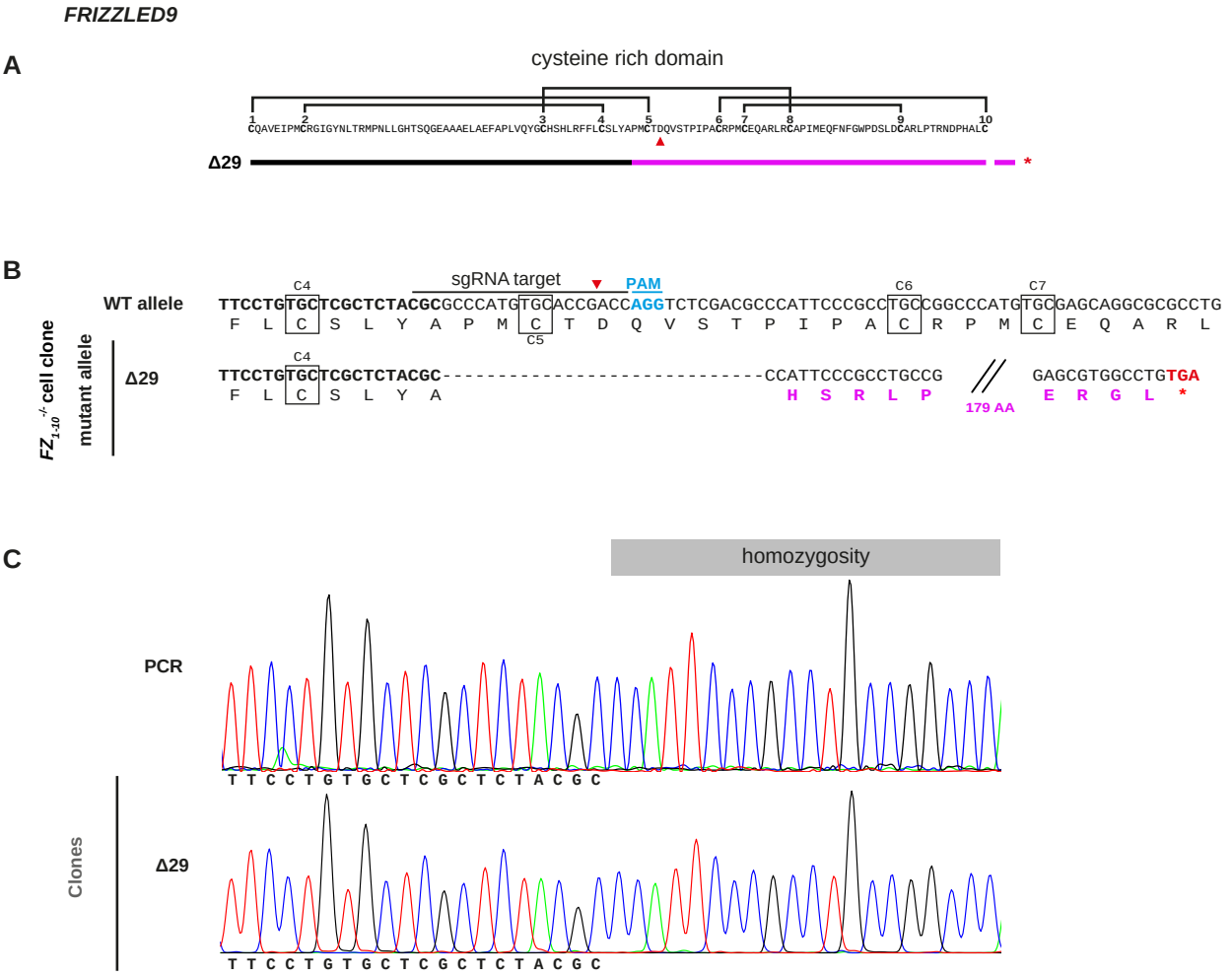

Fig. S1. (continued)

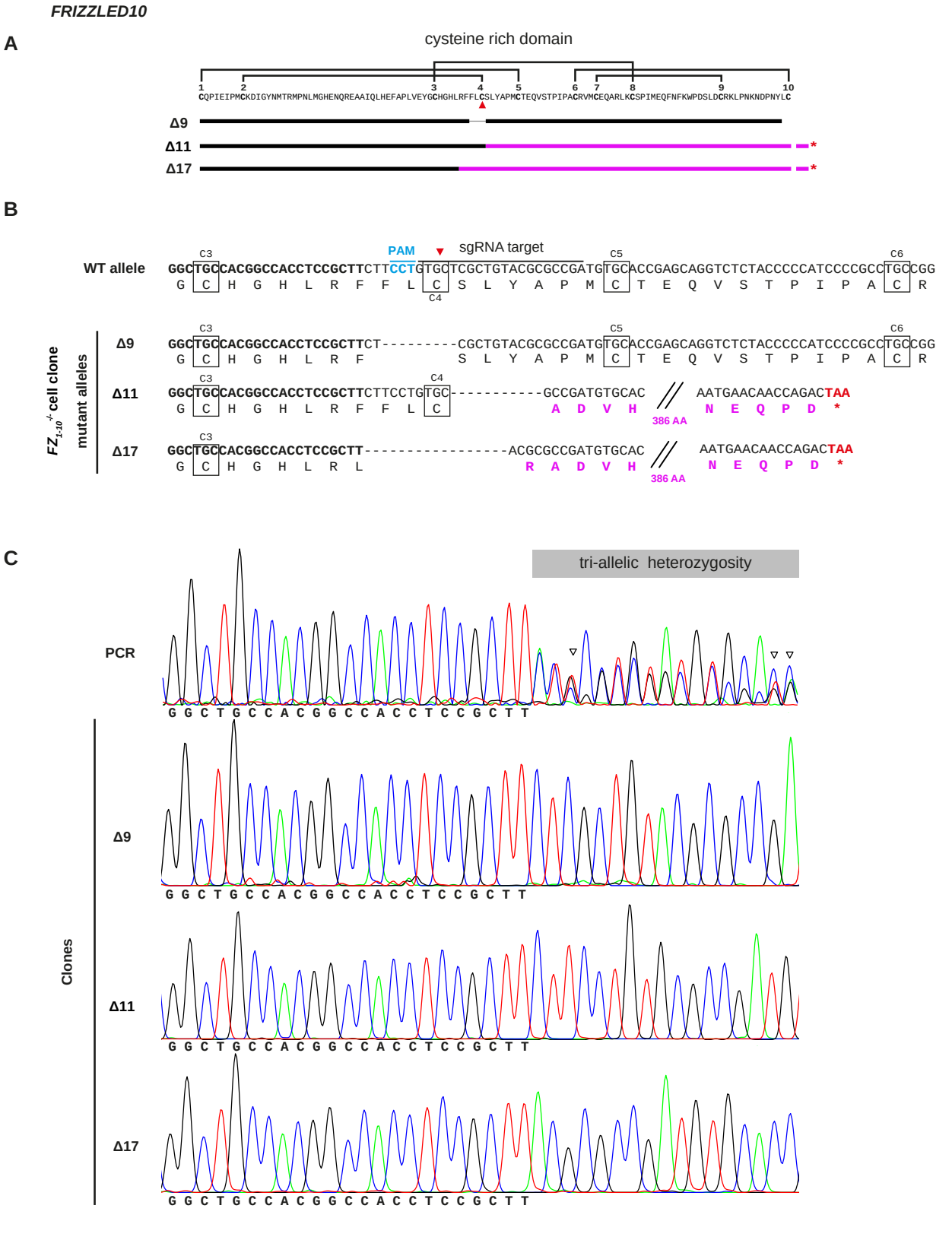

Fig. S1. (continued)

Fig. S1. (continued)

Genetic lesions in $FZ_{1\text{-}10}^{-/-}$ cells.

(A) For each FZ, the amino acid sequence of the CRD is presented at the top. The ten ultraconserved cysteines implicated in the five essential intra-CRD disulfide bridges are numbered and the corresponding disulfide bridges indicated. The red arrowheads show the predicted Cas9 cleavage site. The predicted translation products of the mutant alleles are shown below. (B) The reference nucleotide sequence (WT allele) and corresponding amino acid sequence of each FZ are aligned with the mutant allele sequences. The sequence targeted by the sgRNA as well as the PAM (in blue), the cleavage site (red arrow) and cysteines (in black boxes) are indicated in the reference allele. The altered amino acid sequence due to the nucleotides deletion or insertion leading to a frame-shift, is displayed in bold and pink. Premature stop codons are displayed in red. (C) For each target site, mutations were characterized by Sanger sequencing. The chromatograms of the uncloned PCR product centered on the PAM site and each mutant allele are aligned. Arrowheads point to the triple peaks.

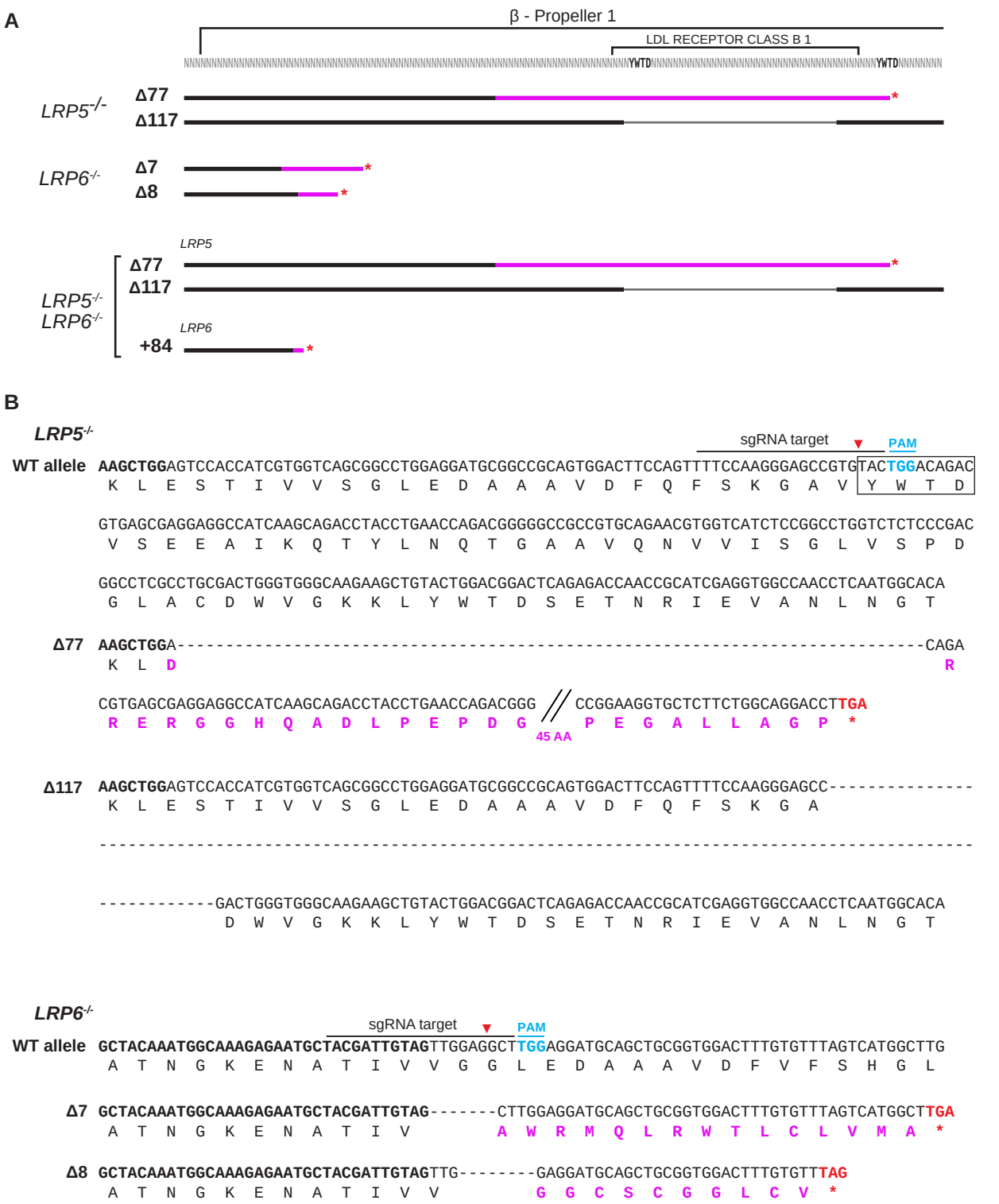
A
β - Propeller 1
LDL RECEPTOR CLASS B 1
YWTD
YWTD
LRP5-/-
Δ77
Δ117
LRP6-/-
Δ7
Δ8
LRP5
LRP5-/-
LRP6-/-
Δ77
Δ117
LRP6
+84
B
LRP5-/-
sgRNA target
PAM
WT allele AAGCTGGAGTCCACCATCGTGGTCAGCGGCCTGGAGGATGCGGCCGCAGTGGACTTCCAGTTTTCCAAGGGAGCCGTGTACTGGACAGAC
K L E S T I V V S G L E D A A A V D F Q F S K G A V Y W T D
GTGAGCGAGGAGGCCATCAAGCAGACCTACCTGAACCAGACGGGGGCCGCCGTGCAGAACGTGGTCATCTCCGGCCTGGTCTCTCCCGAC
V S E E A I K Q T Y L N Q T G A A V Q N V V I S G L V S P D
GGCCTCGCCTGCGACTGGGTGGGCAAGAAGCTGTACTGGACGGACTCAGAGACCAACCGCATCGAGGTGGCCAACCTCAATGGCACA
G L A C D W V G K K L Y W T D S E T N R I E V A N L N G T
Δ77 AAGCTGGA----------CAGA
K L D R
CGTGAGCGAGGAGGCCATCAAGCAGACCTACCTGAACCAGACGGG // CCGGAAGGTGCTCTTCTGGCAGGACCTTGA
R E R G G H Q A D L P E P D G P E G A L L A G P *
45 AA
Δ117 AAGCTGGAGTCCACCATCGTGGTCAGCGGCCTGGAGGATGCGGCCGCAGTGGACTTCCAGTTTTCCAAGGGAGCC----------
K L E S T I V V S G L E D A A A V D F Q F S K G A

----------GACTGGGTGGGCAAGAAGCTGTACTGGACGGACTCAGAGACCAACCGCATCGAGGTGGCCAACCTCAATGGCACA
D W V G K K L Y W T D S E T N R I E V A N L N G T
LRP6-/-
sgRNA target
PAM
WT allele GCTACAAATGGCAAAGAGAATGCTACGATTGTAGTTGGAGGCTTGGAGGATGCAGCTGCGGTGGACTTTGTGTTTAGTCATGGCTTG
A T N G K E N A T I V V G G L E D A A A V D F V F S H G L
Δ7 GCTACAAATGGCAAAGAGAATGCTACGATTGTAG-------CTTGGAGGATGCAGCTGCGGTGGACTTTGTGTTTAGTCATGGCTTGA
A T N G K E N A T I V A W R M Q L R W T L C L V M A *
Δ8 GCTACAAATGGCAAAGAGAATGCTACGATTGTAGTTG--------GAGGATGCAGCTGCGGTGGACTTTGTGTTTAG
A T N G K E N A T I V V G G C S C G G L C V *

Fig. S2.

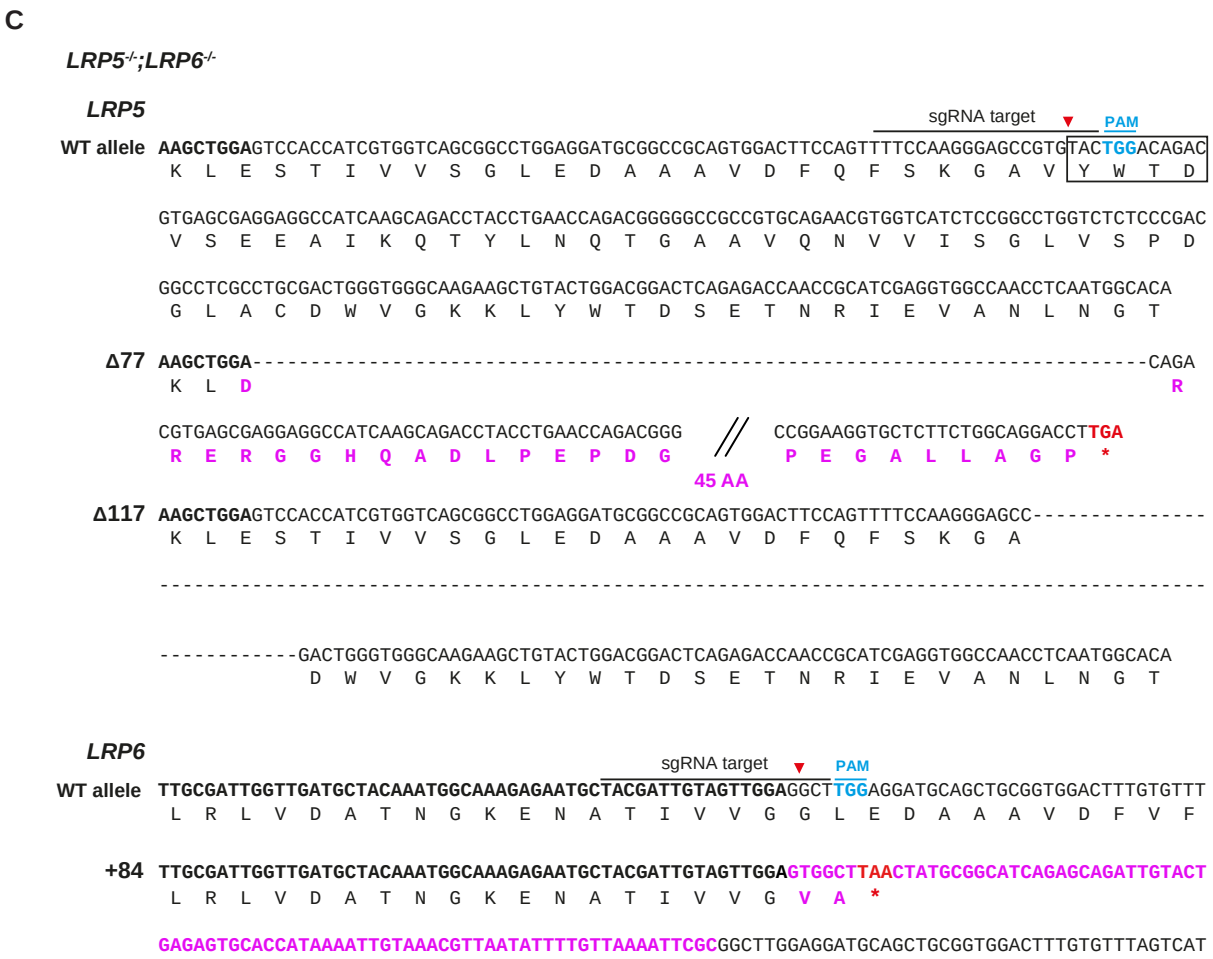

Fig. S2. (continued)

Genetic lesions in *LRP5*$^{-/-}$, *LRP6*$^{-/-}$ and double mutant *LRP5*$^{-/-}$;*LRP6*$^{-/-}$ cells

(A) Schematic representation of the truncated or deleted amino acids sequences in the f rst two YWTD motifs forming the β-propeller structure within LRP5 and LRP6 proteins. (B) Schematic representation of the nucleotide and amino acid sequences of WT *LRP5* and *LRP6* (WT allele) and mutated alleles in the *LRP5*$^{-/-}$ and *LRP6*$^{-/-}$ cell lines. (C) Schematic representation of the nucleotide and amino acid sequences of WT *LRP5* and *LRP6* (WT allele) and mutated alleles in the double mutant *LRP5*$^{-/-}$;*LRP6*$^{-/-}$ cell line. In (B) and (C) the boxes in the WT sequence indicate the YWTD motif. The sequence corresponding to the sgRNA is indicated in the reference allele by the horizontal line, the PAM is in blue, the anticipated double-stranded break site is indicated by the red arrowhead. Frame-shift induced missense amino acid sequences are displayed in bold and pink, inserted nucleotides are displayed in pink and premature stop codons in red.

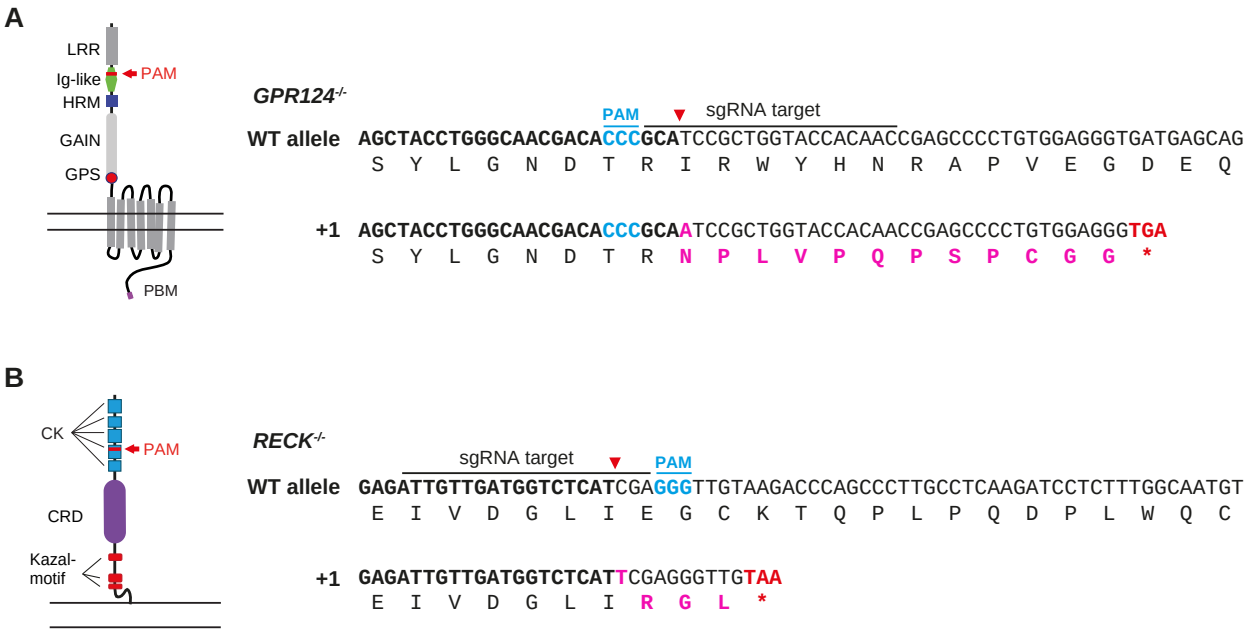

Fig. S3.

Genetic lesions in *GPR124*$^{-/-}$;*RECK*$^{-/-}$ cells.

(A) Schematic illustration of the CRISPR/Cas9 PAM site within the Ig-like domain of Gpr124 and representation of the WT and mutated *GPR124* alleles. (B) Schematic representation of the CRISPR/Cas9 PAM site within the CK4 of RECK and schematic annotation of WT and mutated *RECK* alleles. The sequence corresponding to the sgRNA is indicated in the WT allele by the horizontal line, the PAM is in blue, the anticipated double-stranded break site is indicated by the red arrow. Frame-shift-induced missense amino acid sequences are displayed in pink and bold, inserted nucleotides are displayed in pink and premature stop codons in red.

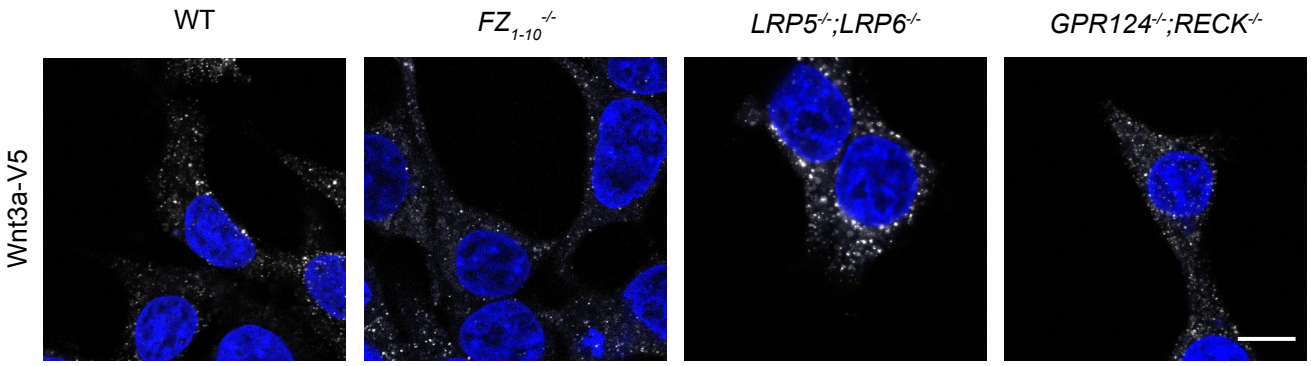

Fig. S4.

Immunodetection of Wnt3a-V5 in *FZ$_{1-10}^{-/-}$*, *LRP5$^{-/-}$;LRP6$^{-/-}$* and *GPR124$^{-/-}$;RECK$^{-/-}$* cells.

Anti-V5 immunofluorescence staining of the ectopically expressed Wnt3a-V5 in WT, *FZ$_{1-10}^{-/-}$*, *LRP5$^{-/-}$;LRP6$^{-/-}$* and *GPR124$^{-/-}$;RECK$^{-/-}$* cells. Scale bar, 10 μm.

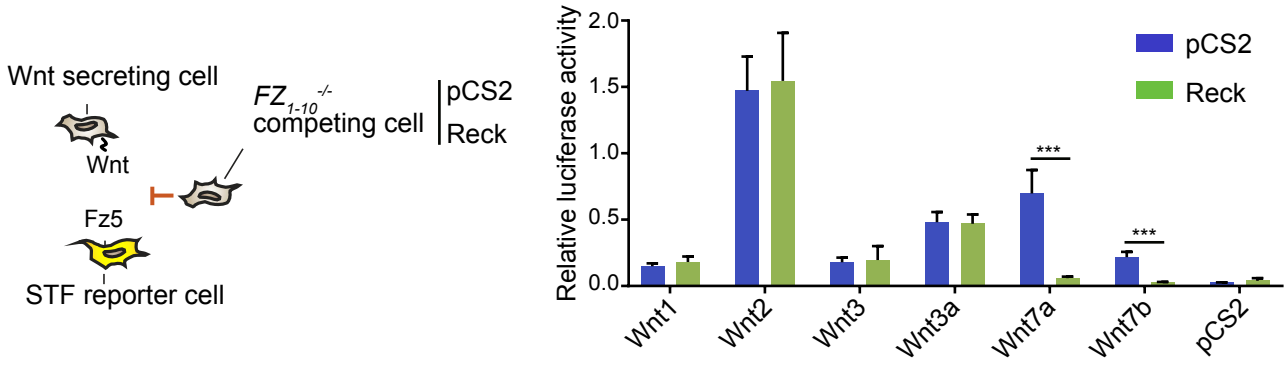

Fig. S5.

Ligand capture assay in triple (1:1:1) co-cultures.

Luciferase activities of HEK293-STF reporter cells transfected with Fz5 (yellow cell) and stimulated in a paracrine manner by co-cultured Wnt-secreting cells in the presence of $FZ_{1\text{-}10}^{-/-}$ HEK293T competing cells transfected with Reck or an empty vector (pCS2). ***$p<0.001$; data represent mean ± SD.

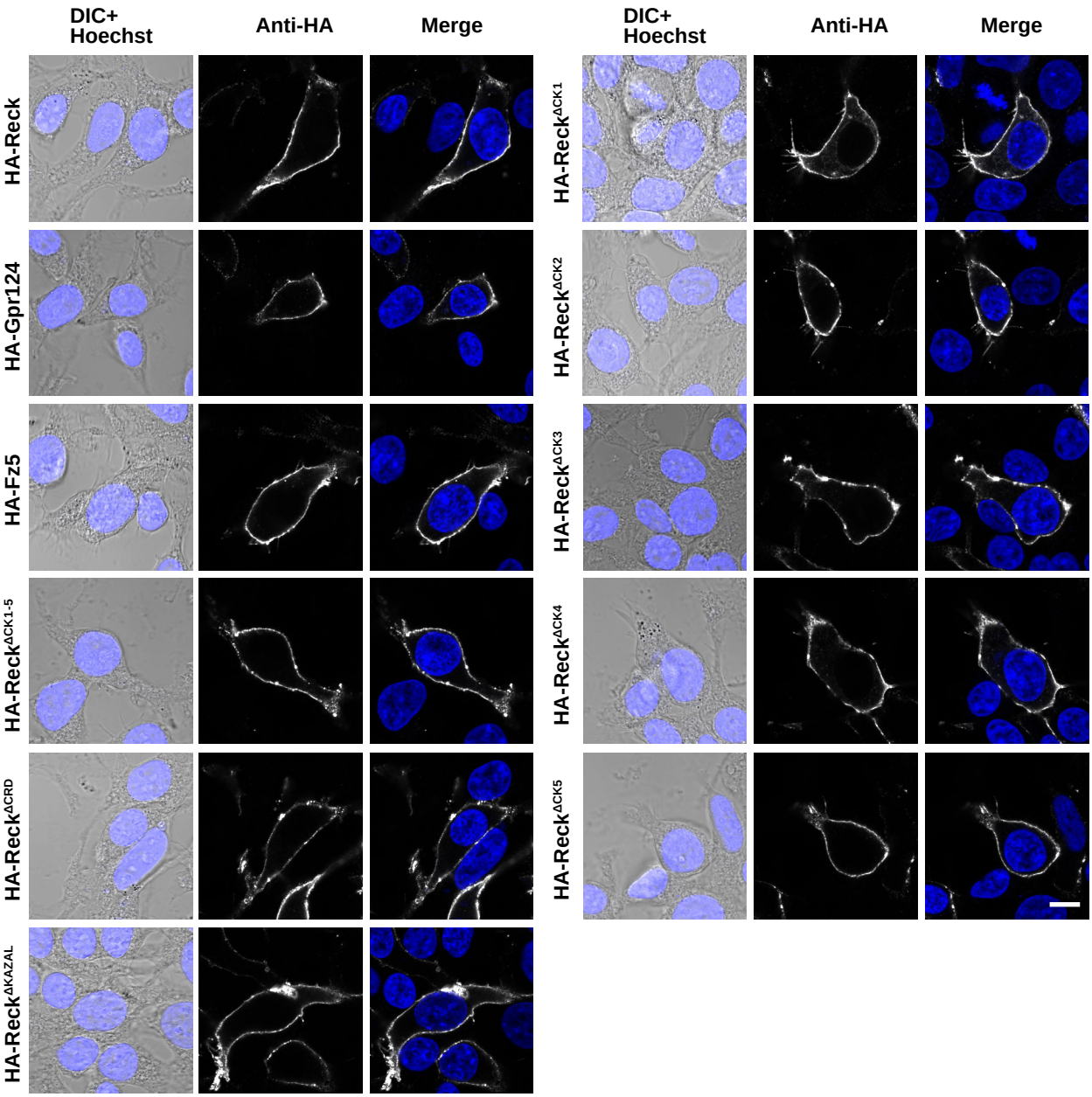

Fig. S6.

Membrane localization of HA-Gpr124, HA-Fz5 and HA-Reck and its variants.

Anti-HA immunofluorescence staining of the indicated HA-tagged receptor component in *GPR124*$^{-/-}$;*RECK*$^{-/-}$ cells. Scale bar, 10 μm.

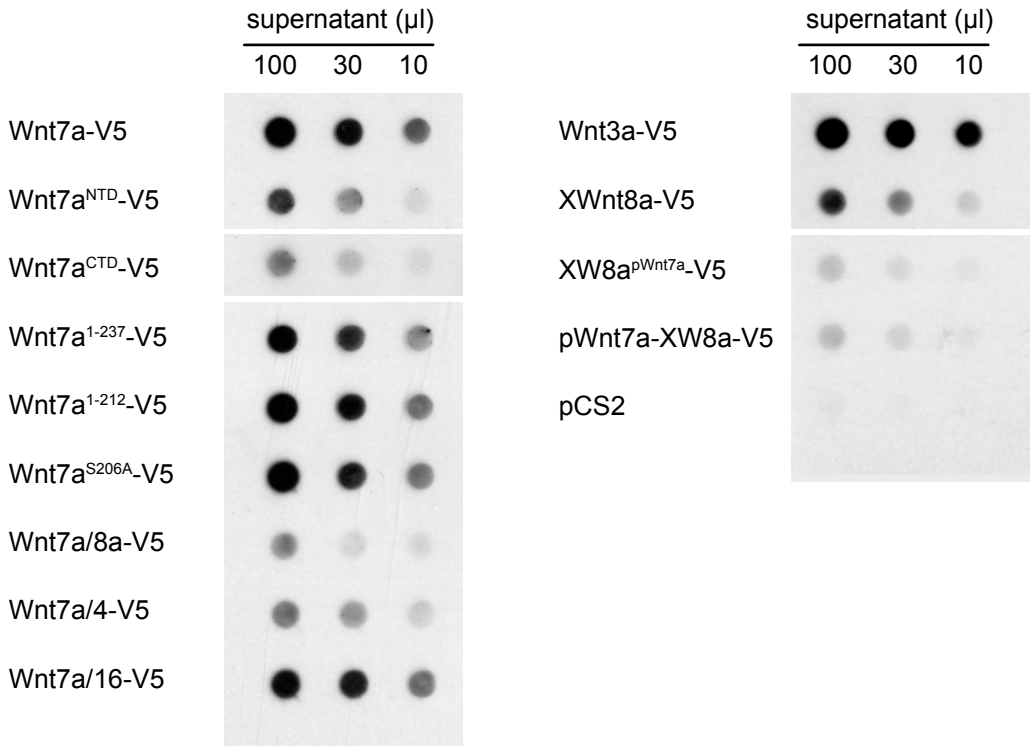

Fig. S7.

Semi-quantitative anti-V5 dot blot analysis of Wnt3a-V5, XWnt8a-V5, Wnt7a-V5 and its variants accumulation in the culture medium.

HEK293T were transfected with the indicated V5-tagged Wnt ligands. 48 h post-transfection, the cell supernatant was absorbed on the membrane using serial dilutions as indicated. The membrane was probed with anti-V5 antibodies.

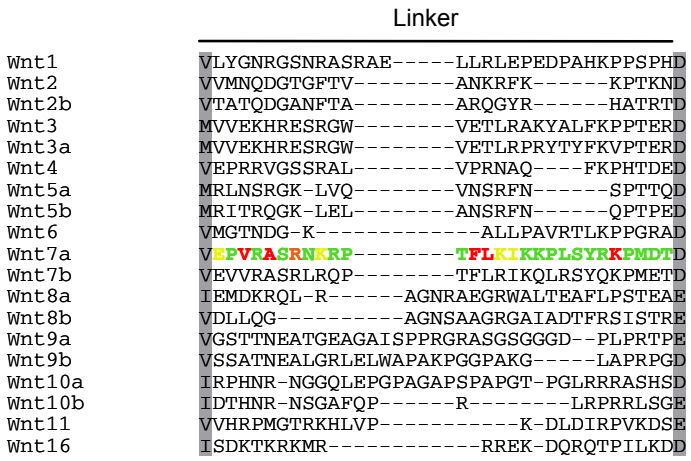

Fig. S8.

Sequence alignment of the linker domains of the 19 mouse Wnt ligands.

Similar residues are highlighted in grey. The residues of Wnt7a are color coded according to the activity class of the corresponding single-residue variants for Gpr124/Reck-dependent signaling as determined in Fig. 2G.

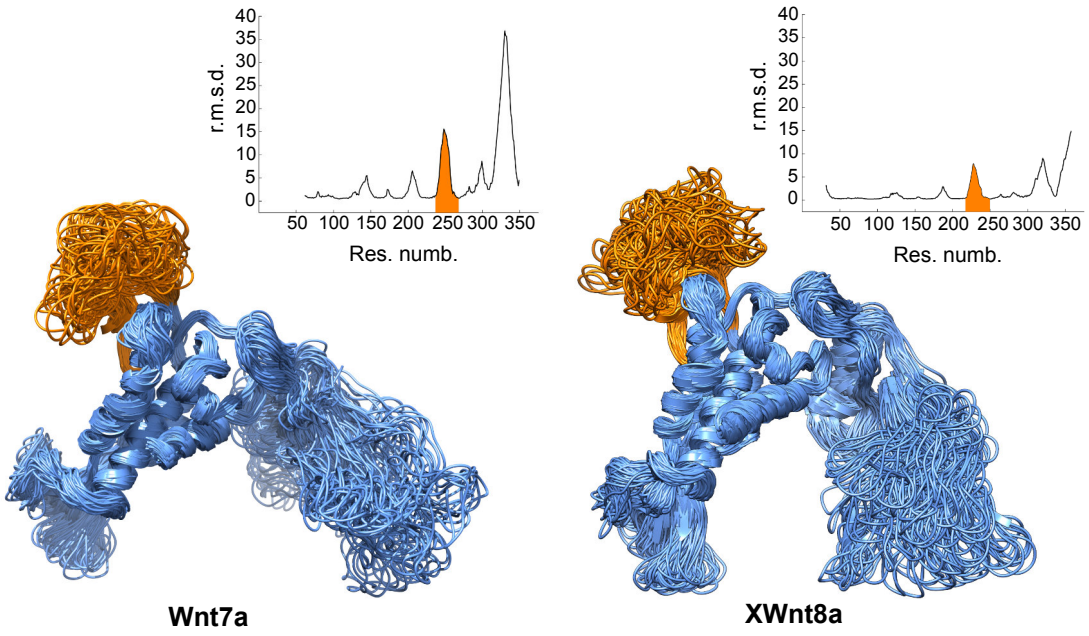

Fig. S9.

Molecular dynamics stimulation of mouse Wnt7a and XWnt8a.

The initial structural models calculated with Rosetta 3.5 were used in a molecular dynamics simulation that was sampled throughout the simulation. The coordinates taken at different times were aligned and compared to detect regions undergoing large structural variations. As shown in the inset the residues highlighted in orange correspond to the Wnt linker regions where large backbone root-mean-square deviation (r.m.s.d.) changes can be detected.

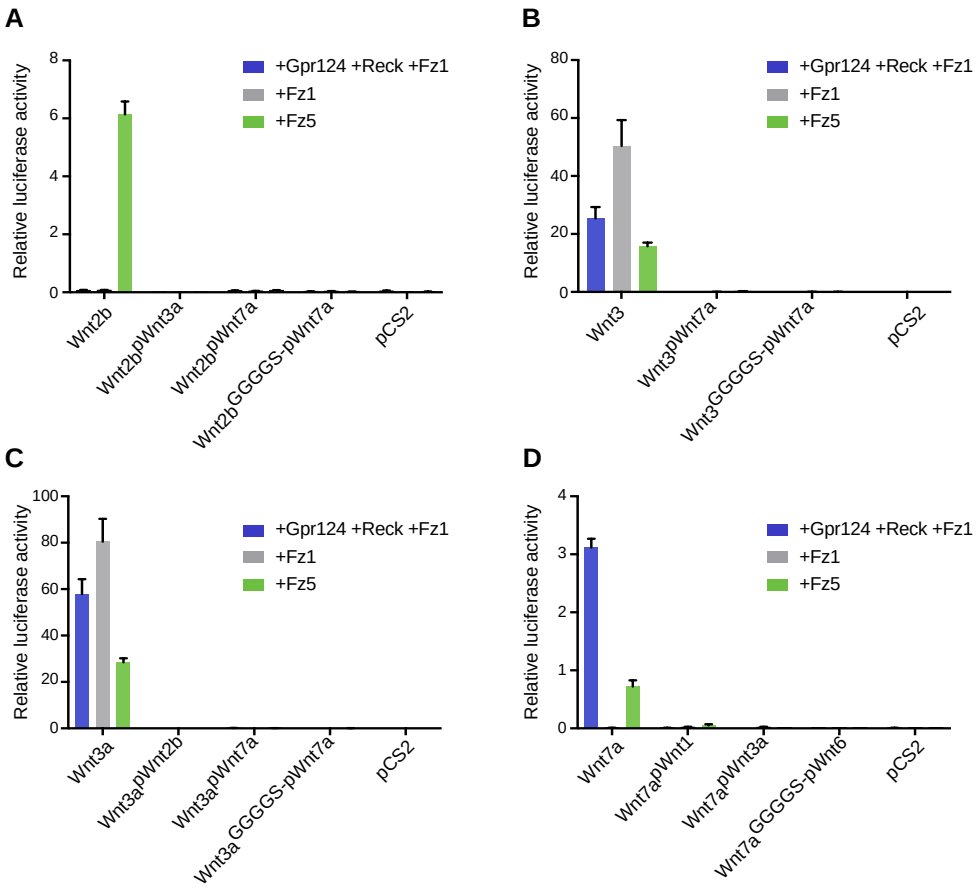

Fig. S10.

Inactivity of the Wnt linker chimeras.

Relative luciferase activity of HEK293-STF co-expressing the indicated Fz receptors and co-receptors together with the linker chimeras of mWnt2b (A), mWnt3 (B), mWnt3a (C) and mWnt7a (D). In these chimeras, the linker is substitued by the linker of the indicated Wnt f anked, or not, on both sides by the f exible GGGGS pentapeptide. Data represent mean ± SD.

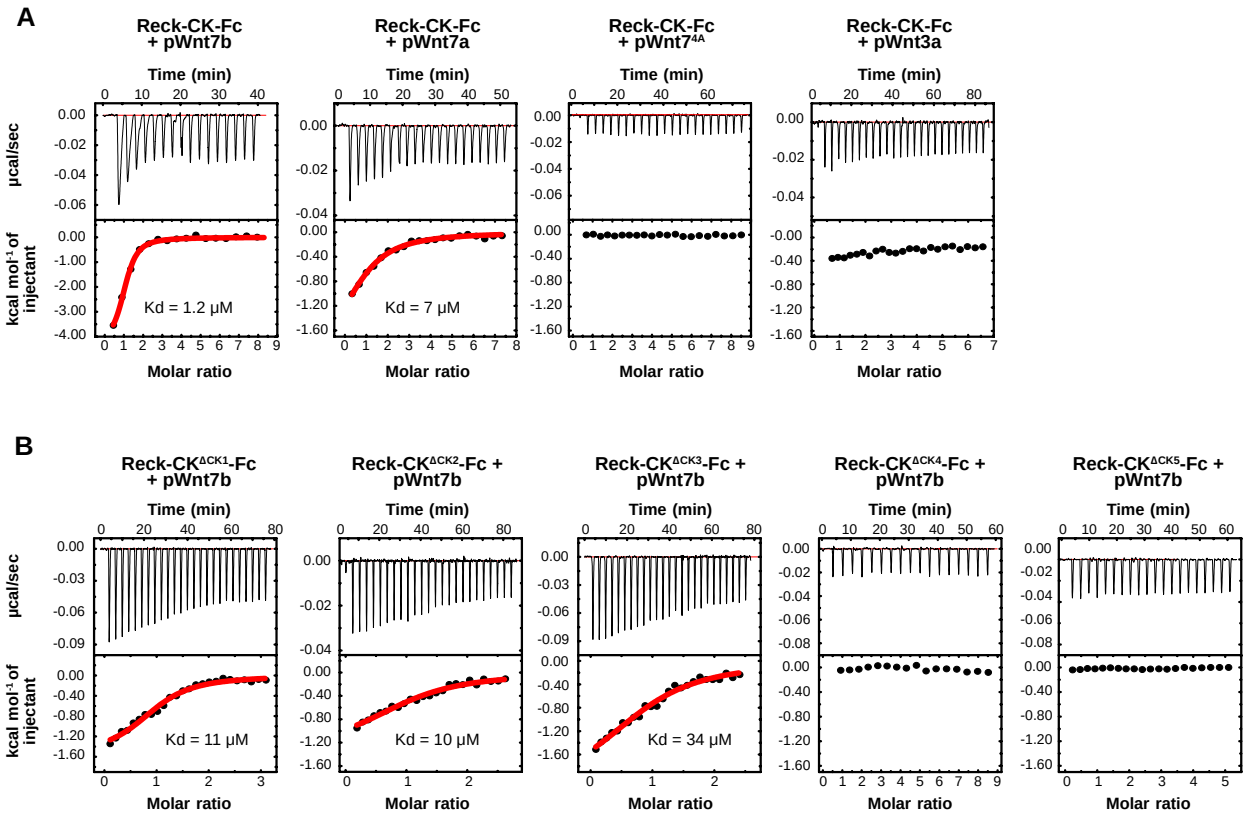

Fig. S11.

Binding of Reck-CK-Fc to Wnt-derived synthetic linker peptides.

(A) Isothermal Titration Calorimetry (ITC) titration curves of pWnt7b, pWnt7a, pWnt7a^{4A} and pWnt3a into Reck-CK-Fc. (B) ITC titration of Reck-CK$^{\Delta CK1}$-Fc, Reck-CK$^{\Delta CK2}$-Fc, Reck-CK$^{\Delta CK3}$-Fc, Reck-CK$^{\Delta CK4}$-Fc and Reck-CK$^{\Delta CK5}$-Fc to pWnt7b.

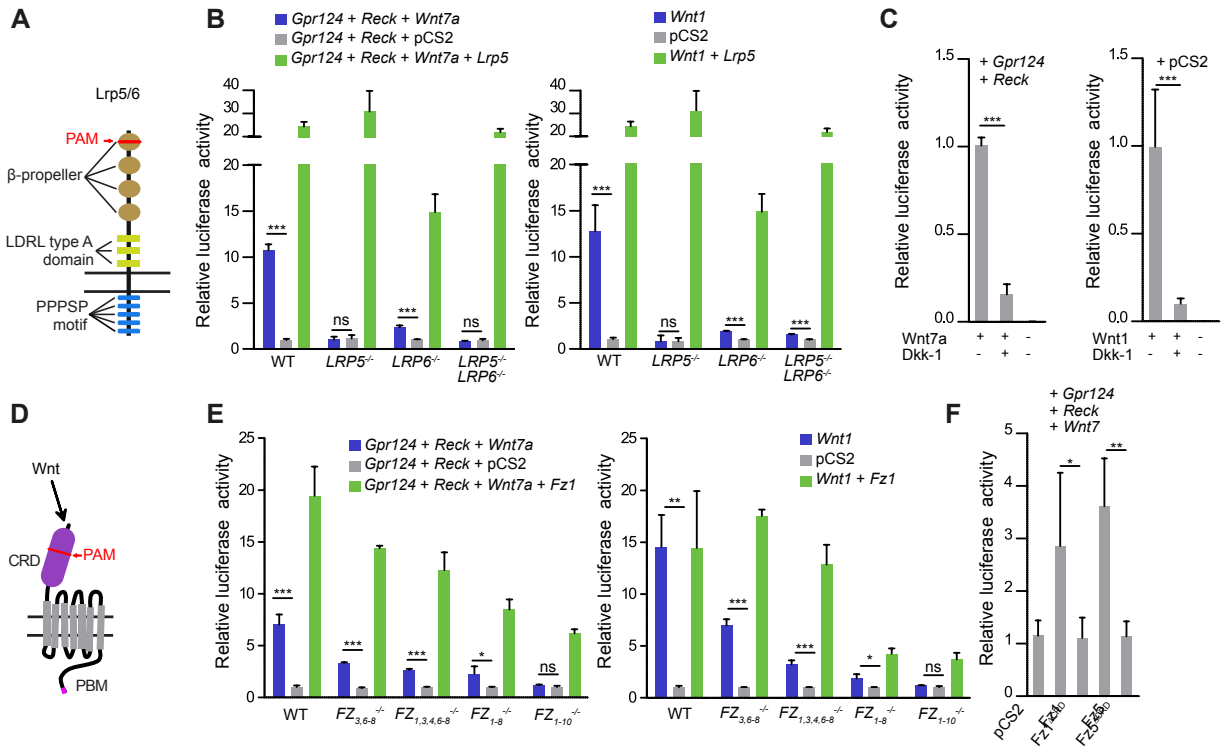

Fig. S12.

Characterization of Gpr124/Reck signaling in *LRP5/6* and *FZ* knock-out cell lines.

(A) Schematic illustration of the CRISPR/Cas9 PAM site in Lrp5/6. (B) Luciferase activities in WT HEK293T cells, *LRP5*$^{-/-}$, *LRP6*$^{-/-}$ or double mutant *LRP5*$^{-/-}$;*LRP6*$^{-/-}$ HEK293T cell clones 48 h after transfection with the indicated combinations of plasmids together with STF reporter plasmids, stimulating either Reck/Gpr124-dependent Wnt7a signaling or Gpr124/Reck-independent Wnt1 signaling. (C) STF activity of Gpr124/Reck-dependent and -independent signaling in WT HEK293T cells in the presence or absence of co-expressed Dkk-1. (D) Schematic representation of the CRISPR/Cas9 PAM site within Fz CRD. (E) Luciferase activities in WT HEK293T cells or *FZ* mutant HEK293T cell clones 48 h after transfection with STF reporter plasmids together with the indicated combinations of expression plasmids, stimulating Reck/Gpr124-dependent Wnt7a signaling or Gpr124/Reck-independent Wnt1 signaling. (F) STF activity of Gpr124/Reck-dependent signaling in $FZ_{1\text{-}10}^{-/-}$ HEK293T after co-transfection with the indicated Fz or Fz CRD variant. *p<0.05, **p<0.01, ***p<0.001; data represent mean ± SD.

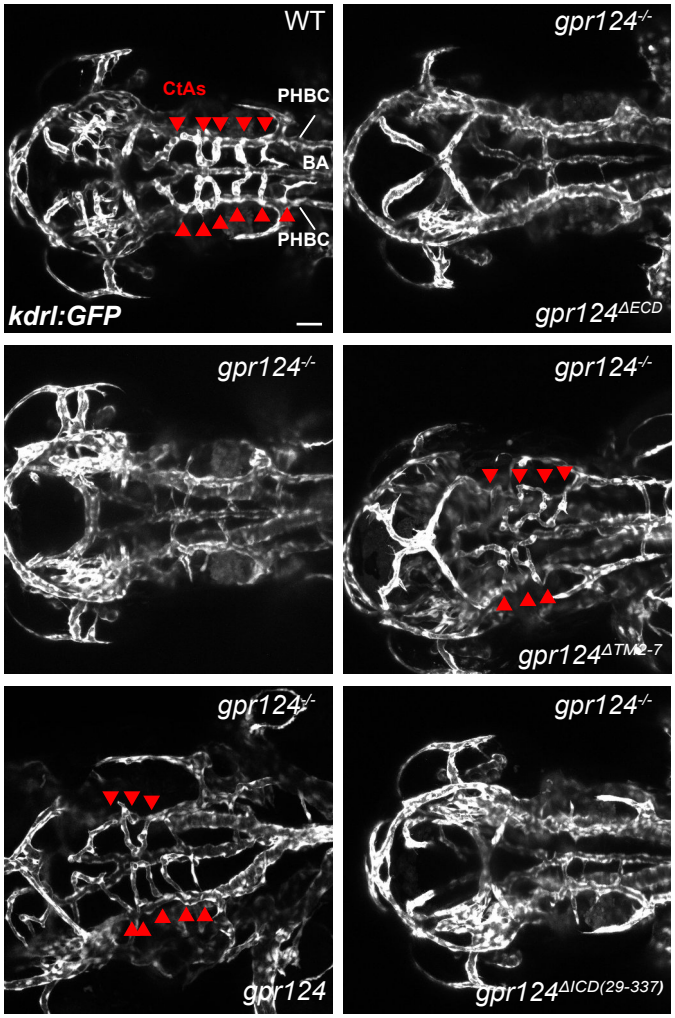

Fig. S13.

Confocal stacks of the cranial vasculature of WT or *gpr124* mutant embryos injected with *gpr124, gpr124$^{\Delta ECD}$, gpr124$^{\Delta TM2-7}$ and gpr124$^{\Delta ICD(29-337)}$*.

Cranial vasculature of 60 hpf WT and *gpr124* mutant embryos injected at the one-cell stage with 100 pg of the indicated mRNAs. CtA, Central Artery; BA, Basilar Artery; PHBC, Primordial Hindbrain channel. Red arrowheads point to CtAs. Scale bar, 50 μm.

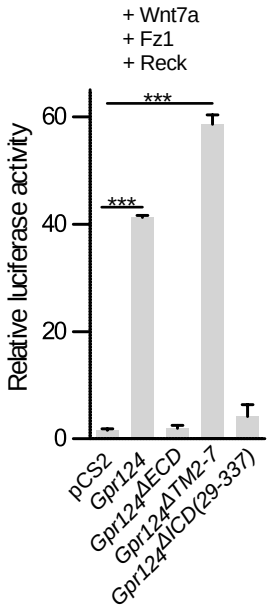

Fig. S14.

***In vitro* STF activity of Gpr124 and its variants.**

Relative luciferase activity of HEK293-STF cells co-transfected with Reck, Fz1, Wnt7a and the indicated Gpr124 variants. ***$p<0.001$; data represent mean ± SD.

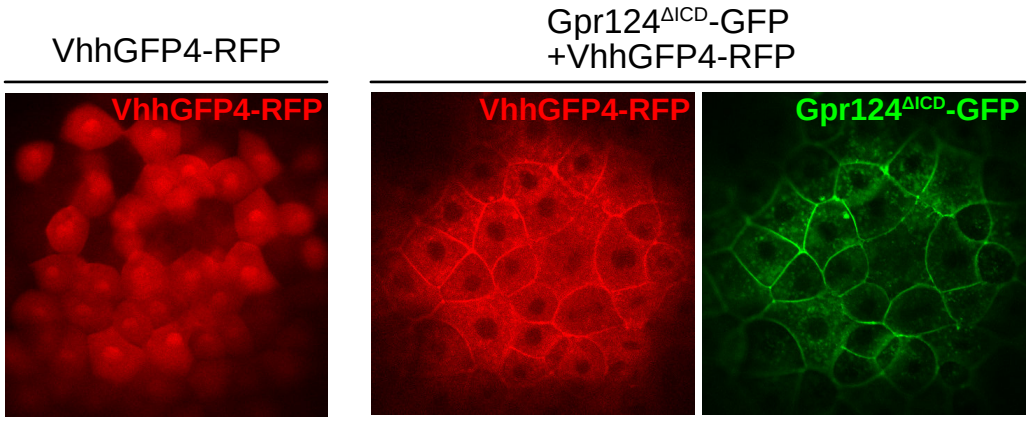

Fig. S15.

Validation of the nanobody-based bimolecular complementation assay.

Single-plane confocal scans through enveloping layer cells of 5 hpf zebraf sh blastula injected with *VhhGFP4-RFP* mRNA alone or in combination with *Gpr124$^{\Delta ICD}$-GFP* mRNA.

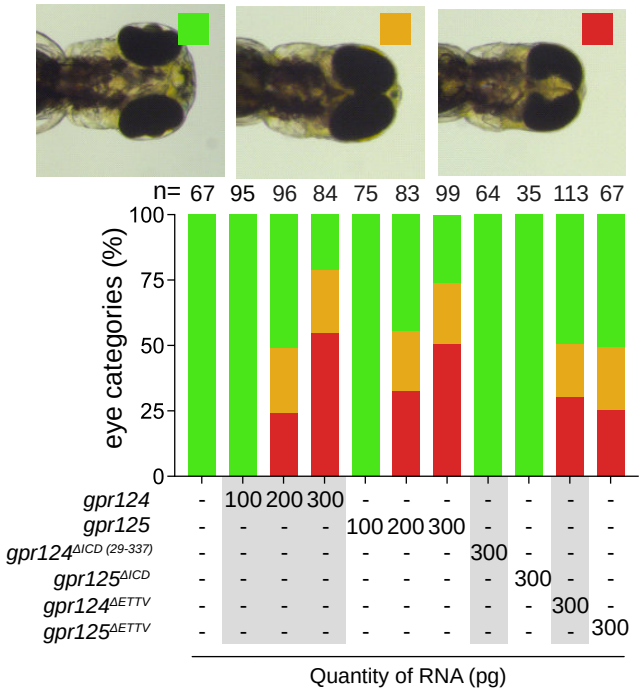

Fig. S16.

Quantif cation of eye fusion phenotypes.

Embryos injected with the indicated mRNA amounts of *gpr124*, *gpr125* or their variants were scored according to their eye fusion phenotypes. Eye fusions were categorized in three classes (represented in the three ventral views of embryos): green (no fusion), orange (synophthalmia) and red (cyclopia).

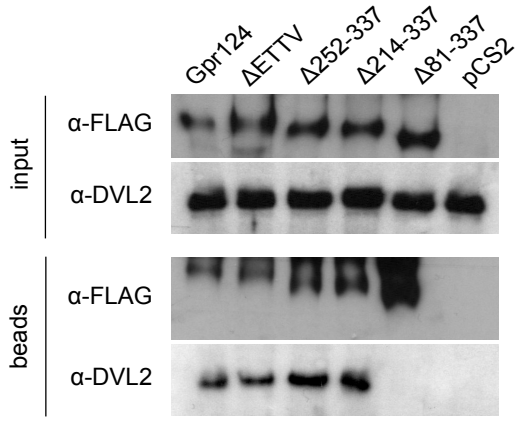

Fig. S17.

Interaction between Gpr124 and endogenous DVL2.

Anti-FLAG co-immunoprecipitation assays performed in total lysates of $FZ_{1\text{-}10}^{-/-}$ cells expressing N-terminal FLAG-tagged versions of Gpr124 and its ICD variants. Input lysates and IP samples are probed with anti-DVL2 and anti-FLAG antibodies.

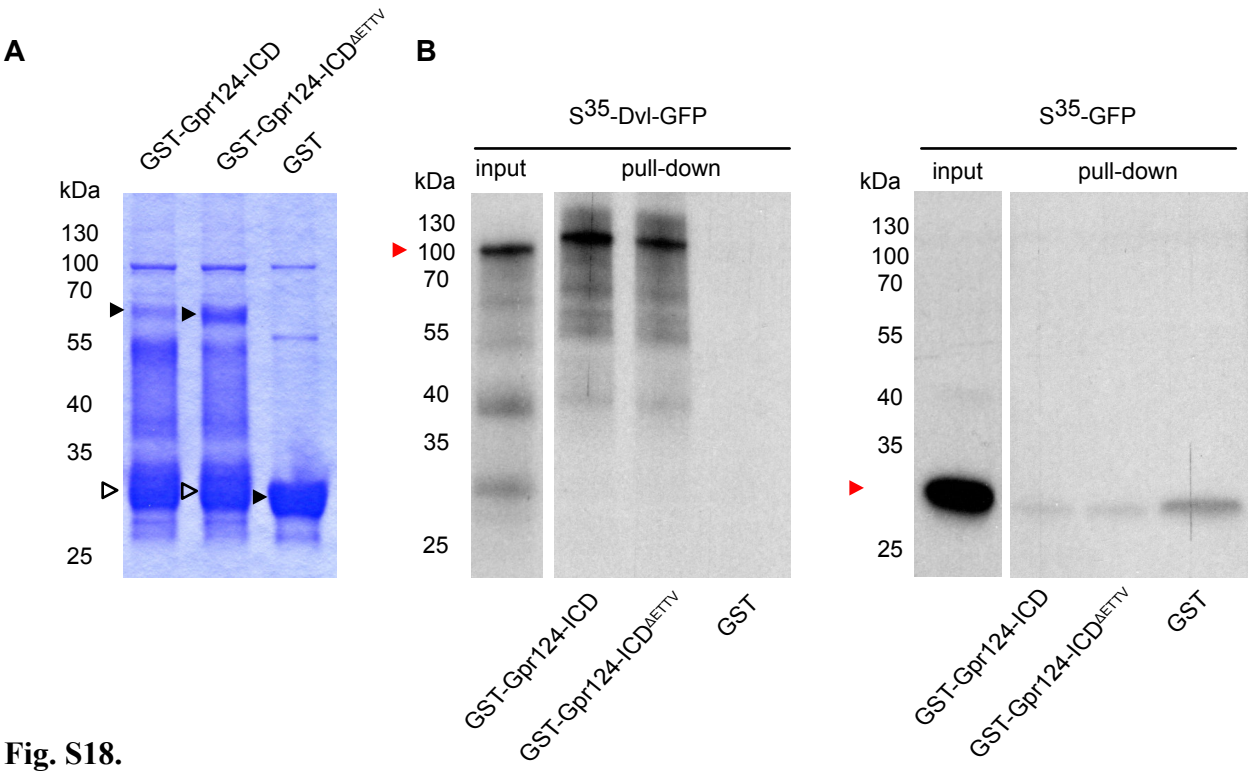

Fig. S18.

Characterization of the Dvl – Gpr124^{ICD} interaction by GST pull-downs.

(A) Gpr124 ICD variants were produced as N-terminal GST fusion proteins in *E.coli* and purified on Glutathione Sepharose beads. The full-length GST fusion products of expected size are indicated by filled arrowheads while open arrowheads point to cleaved or uncomplete GST translational products on Coomassie blue staining. The immobilized recombinant proteins were incubated overnight with S^{35}-labelled *in vitro* translated GFP or Dvl-GFP fusions. (B) Pull-downs were analyzed using SDS-page and fluorography. Red arrowheads point to GFP and Dvl-GFP in the input and pull-down samples.

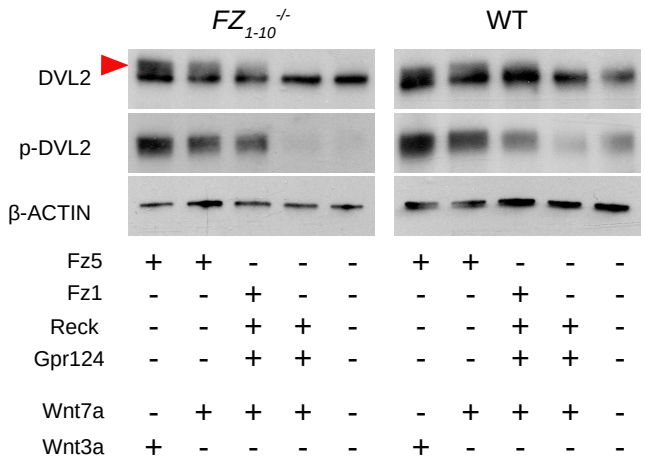

Fig. S19.

Immunoblot of DVL2 and p-DVL2 in whole cell lysates from *FZ*$_{1\text{-}10}^{-/-}$ and WT HEK293T cells.

Immunoblot of DVL2 and p-DVL2 (T224) in whole cell lysates from *FZ*$_{1\text{-}10}^{-/-}$ and WT HEK293T cells transfected with the indicated combination of plasmids. Phosphorylated DVL2 (T224) could be detected as a slowly migrating band with anti-DVL2 antibodies (red arrowhead) or by a phosphospecif c antibody recognizing phosphothreonine 224 (p-DVL2) in whole cell extracts obtained after 48 h post-transfection with the different combinations of constructs as indicated. Note the absence of p-DVL2 in *FZ*$_{1\text{-}10}^{-/-}$ cells transfected with Gpr124, Reck and Wnt7a.

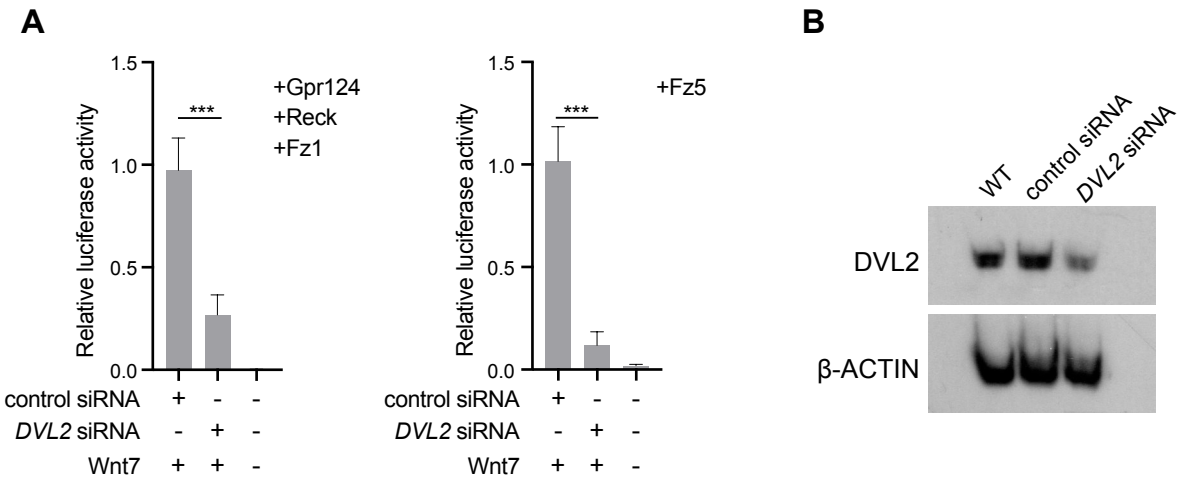

Fig. S20.

Depletion of *DVL2* by siRNA impairs Gpr124/Reck and Fz5 signaling.

(A) HEK293-STF cells were transfected with the indicated combination of plasmids and control or *DVL2* siRNAs. STF luciferase reporter activity was measured after 48 hours. (B) The level of the endogenous DVL2 protein was assessed by western blotting of total cell lysates. ***$p<0.001$; data represent mean ± SD.

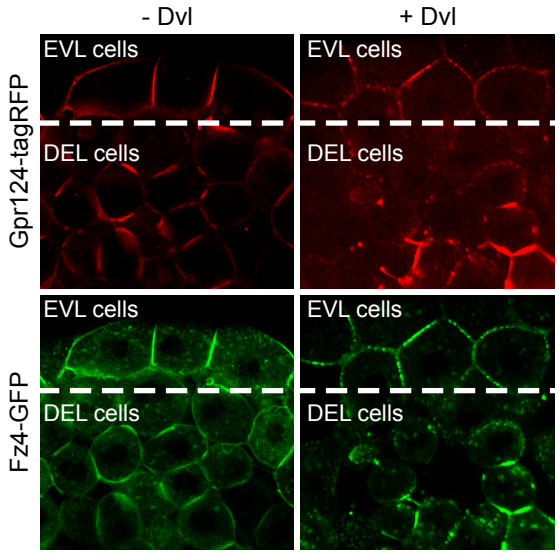

Fig. S21.

Intracellular distribution of co-expressed Fz4-GFP and Gpr124-tagRFP in the absence or the presence of Dvl in zebrafish blastula.

Single-plane xy confocal scans through 5 hpf zebrafish blastula co-injected with Gpr124-tagRFP and Fz4-GFP with or without Dvl. In peripheral EVL monolayer, cells exhibit continuous cell contacts, while internal DEL cells of the bastula exhibit more discrete contact sites.

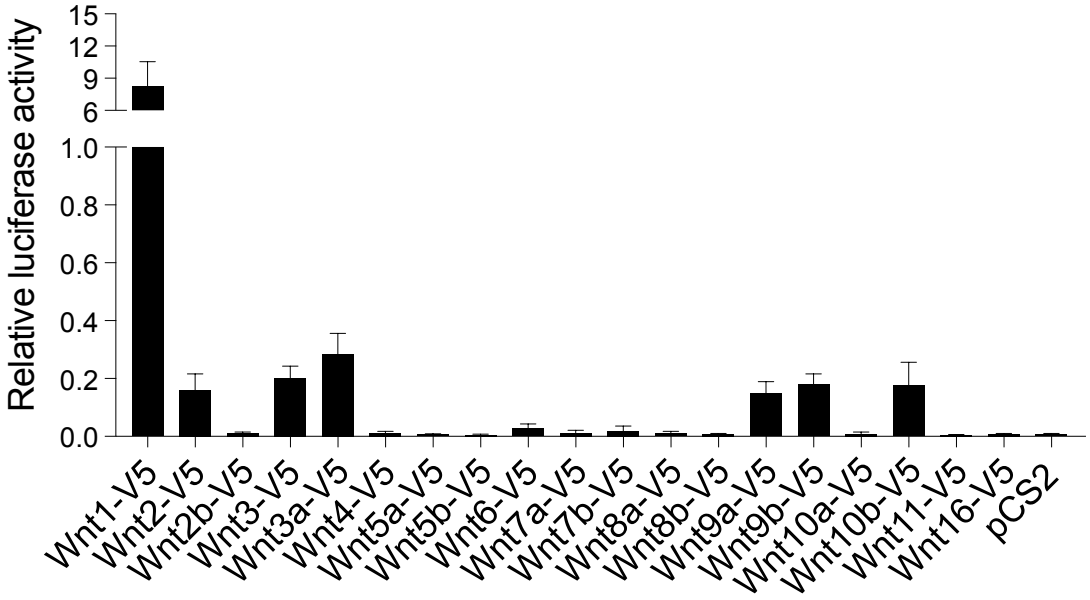

Fig. S22.

Activity of the V5 tagged Wnt proteins.

The 19 human V5-tagged Wnt ligands were transfected in HEK293 - STF cells. STF luciferase reporter activity was measured after 48 h.

Genes	Alleles	*clones from PCR A*	*clones from PCR B*	Total of reads
FZ1	Δ 2	3	3	6
	Δ 8	4	4	8
	Δ 33	2	8	10
FZ2	Δ 2	4	4	8
FZ3	Δ 8	2	5	7
	Δ 17	2	6	8
FZ4	+ 1	5	5	10
FZ5	Δ 11	5	2	7
	Δ 76	5	3	8
FZ6	Δ 5 + 13	2	3	5
	Δ 20	3	2	5
FZ7	+ 2	4	6	10
	Δ 1	5	15	20
	Δ 89 + 81	2	27	29
FZ8	Δ 15	4	2	6
	Δ 6	6	7	13
FZ9	Δ 29	3	5	8
FZ10	Δ 9	5	2	7
	Δ 11	4	2	6
	Δ 17	6	7	13

Table S1.

Analysis of the $FZ_{1\text{-}10}^{-/-}$ cell line through Sanger sequencing.

For each *FZ* gene, two independent PCR products (A and B) centered on the PAM site were sequenced and subsequently cloned as described in the Materials and Methods. The number of sequenced clones for each *FZ* allelle is indicated.